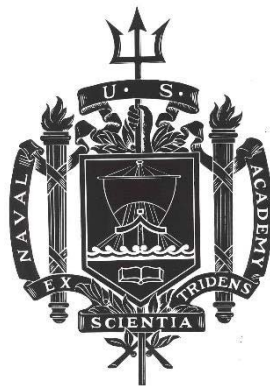# A TRIDENT SCHOLAR PROJECT REPORT

NO. 478

Design of a hand exoskeleton system actuated via linear and adaptive control for rehabilitation
by

Midshipman 1/C Anderson S. Camp, USN

UNITED STATES NAVAL ACADEMY
ANNAPOLIS, MARYLAND

REPORT DOCUMENTATION PAGE

Form Approved
OMB No. 0704-0188

1. REPORT DATE *(DD-MM-YYYY)* 5-20-19	2. REPORT TYPE	3. DATES COVERED *(From - To)*

4. TITLE AND SUBTITLE

Design of a Hand Exoskeleton System Actuated via Linear and Adaptive Control for Rehabilitation

5a. CONTRACT NUMBER

5b. GRANT NUMBER

5c. PROGRAM ELEMENT NUMBER

6. AUTHOR(S)

Camp, Anderson S.

5d. PROJECT NUMBER

5e. TASK NUMBER

5f. WORK UNIT NUMBER

7. PERFORMING ORGANIZATION NAME(S) AND ADDRESS(ES)

8. PERFORMING ORGANIZATION REPORT NUMBER

9. SPONSORING / MONITORING AGENCY NAME(S) AND ADDRESS(ES)

U.S. Naval Academy
Annapolis, MD 21402

10. SPONSOR/MONITOR'S ACRONYM(S)

11. SPONSOR/MONITOR'S REPORT NUMBER(S)

Trident Scholar Report no. 478 (2019)

12. DISTRIBUTION / AVAILABILITY STATEMENT

This document has been approved for public release; its distribution is UNLIMITED.

13. SUPPLEMENTARY NOTES

14. ABSTRACT

A hand exoskeleton is designed and constructed to achieve five hand positions: (1) fully extended, (2) hook fist, (3) right angle to the palm, (4) straight fist, and (5) fully flexed. These hand orientations comprise the five positions defining a rehabilitation exercise known as tendon glide. The device is significant in its ability to move the two joints distal to the palm independently of the joint adjoining the palm, without requiring bulky, rigid hardware located on the finger. Movement of the finger is achieved through hydraulically activated fluidic artificial muscles (FAMs). FAMs are soft, biomimetic actuators consisting of an expandable bladder encased in a braided sheath. FAMs show improved force-to-weight ratios, cost, and alignment strategies over traditional, rigid hydraulic cylinders and allow forces to be applied across a flexed joint of the finger as it straightens. A direct model of the relationship between the volume transferred to the FAM by the hydraulic cylinder and the strain of the FAM is developed and validated through experiment. The strain-volume relationship remains constant regardless of load, enabling streamlined models and control algorithms. Position-based control of the FAMs is achieved, in both simulation and experiment, with a Proportional Integral (PI) controller and a Model Reference Adaptive Controller (MRAC). The PI controller is a linear algorithm characterized by constant controller gains. Alternatively, MRAC is an adaptive control algorithm characterized by time-varying controller gains, which can guarantee convergence of the actual system to a defined reference system. The resultant device is a wearable exoskeleton actuated by FAMs and governed by novel control architecture. The exoskeleton is capable of guiding a finger through all five positions of tendon glide. The exoskeleton aims to assist patients with at-home rehabilitation, particularly targeting patients who are typically unable to conduct their exercises without assistance from an occupational therapist.

15. SUBJECT TERMS

McKibben, FAM, hydraulics, rehabilitation, exoskeleton

16. SECURITY CLASSIFICATION OF:			17. LIMITATION OF ABSTRACT	18. NUMBER OF PAGES	19a. NAME OF RESPONSIBLE PERSON
a. REPORT	**b. ABSTRACT**	**c. THIS PAGE**		67	**19b. TELEPHONE NUMBER** *(include area code)*

Standard Form 298 (Rev. 8-98)
Prescribed by ANSI Std. Z39.18

Design of a hand exoskeleton system actuated via linear and adaptive control for rehabilitation

by

Midshipman 1/C Anderson S. Camp
United States Naval Academy
Annapolis, Maryland

_____
(signature)

Certification of Adviser(s) Approval

Assistant Professor Paola Jaramillo Cienfuegos
Weapons, Robotics and Control Department

_____
(signature)

_____
(date)

LCDR Edward M. Chapman, USN
Physics Department

_____
(signature)
_____
(date)

Acceptance for the Trident Scholar Committee

Professor Maria J. Schroeder
Associate Director of Midshipman Research

_____
(signature)
_____
(date)

USNA-1531-2

Abstract

A hand exoskeleton is designed and constructed to achieve five hand positions: (1) fully extended, (2) hook fist, (3) right angle to the palm, (4) straight fist, and (5) fully flexed. These hand orientations comprise the five positions defining a rehabilitation exercise known as tendon glide. The device is significant in its ability to move the two joints distal to the palm independently of the joint adjoining the palm, without requiring bulky, rigid hardware located on the finger. Movement of the finger is achieved through hydraulically activated fluidic artificial muscles (FAMs). FAMs are soft, biomimetic actuators consisting of an expandable bladder encased in a braided sheath. FAMs show improved force-to-weight ratios, cost, and alignment strategies over traditional, rigid hydraulic cylinders and allow forces to be applied across a flexed joint of the finger as it straightens. A direct model of the relationship between the volume transferred to the FAM by the hydraulic cylinder and the strain of the FAM is developed and validated through experiment. The strain-volume relationship remains constant regardless of load, enabling streamlined models and control algorithms. Position-based control of the FAMs is achieved, in both simulation and experiment, with a Proportional Integral (PI) controller and a Model Reference Adaptive Controller (MRAC). The PI controller is a linear algorithm characterized by constant controller gains. Alternatively, MRAC is an adaptive control algorithm characterized by time-varying controller gains, which can guarantee convergence of the actual system to a defined reference system. The resultant device is a wearable exoskeleton actuated by FAMs and governed by novel control architecture. The exoskeleton is capable of guiding a finger through all five positions of tendon glide. The exoskeleton aims to assist patients with at-home rehabilitation, particularly targeting patients who are typically unable to conduct their exercises without assistance from an occupational therapist.

keywords: McKibben, FAM, hydraulics, rehabilitation, exoskeleton

1 Acknowledgements

Contents

2 Introduction

Modern rehabilitation techniques have demonstrated the advantageous role technology plays in rehabilitation, particularly for victims of stroke [Thielbar et al., 2014, Volpe et al., 1999, Borboni et al., 2017]. Between 2000 and 2008 the estimated stroke incidence rate in high-income countries was 94 per 100,000 person-year, and approximately 80% of victims survived their stroke in the short term [Feigin et al., 2009]. At least 35% of stroke survivors undergoing rehabilitation who

suffered from some form of mild paresis, paresis, or paralysis recovered motor function to some degree at periods longer than two weeks post-stroke [Hendricks et al., 2002]. Therefore, there is a large population of stroke victims who have the potential to benefit from assistive-rehabilitative technology to aid in their recovery. This research aims to construct an exoskeleton governed by controllers and driven by soft robotic actuators.

Soft robotic actuators vary in construction and method of activation [Laschi and Cianchetti, 2014]. As a group, they are often lightweight, inexpensive, and can be utilized in multiple system alignments. Such actuators have been shown to be effective in lightweight climbing [Chapman et al., 2017], walking [Asbeck et al., 2015], and prosthetic/orthotic devices [Polygerinos et al., 2015, McConnell et al., 2017]. Traditional rigid robotics have been seen in devices for applications ranging from military [Wooden et al., 2010] to clinical [Ruszkowski et al., 2015], but often face limitations when interfacing with the human body. In rehabilitation devices, the use of rigid links in exoskeletons requires the highly sensitive alignment of joints [Polygerinos et al., 2015] and inefficient mechanical stops to prevent injury. Additionally, rigid robots tend to be expensive and heavier than soft robotic systems [Polygerinos et al., 2015]. Soft robots are able to take advantage of the morphology of the body due to their compliant nature. The inherent advantage allows for simplified construction of a robotic system [Polygerinos et al., 2015]. In exoskeleton applications, soft actuators can often apply force across the biological joint without the need for alignment [Asbeck et al., 2015, Chapman and Bryant, 2018].
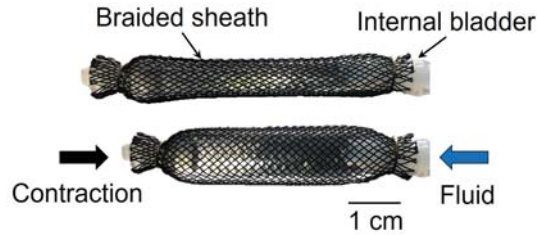
Figure 1: Contraction of a fluidic artificial muscle. Pressure from the fluid causes the internal bladder to expand, leading the muscle to contract.

Soft, tensile actuators are often akin to variable stiffness springs and can replicate the mechanical function of biological skeletal muscle, as skeletal muscle employs similar actuation techniques to cause motion [Pfeifer et al., 2012]. One such type of variable stiffness artificial muscle is the fluidic artificial muscle (FAM). There are a wide range of artificial muscles categorized as FAMs. The FAM shown in Figure 1 is considered here. This early-stage artificial muscle was developed for use as an arm-and-hand orthotic for polio patients and is often named for the designer of its control valve, Joseph McKibben, whose daughter suffered from polio. The McKibben FAM design dates to the 1950's [Tondu, 2012] and is distinctive in its high force to weight ratio. The muscle is constructed of an inner bladder, made of an elastic material such as latex, surrounded by a braided sheath, often constructed of a nylon or Kevlar© mesh. When an internal source pressure is applied to the FAM, the inner bladder is forced to expand, transmitting the force to the braided sheath. The sheath prevents the bladder from lengthening and acts to translate radial expansion to axial contraction. Recent improvements in computer modeling capabilities have led to a resurgence in the study of these actuators [Meller et al., 2014, Tondu and Lopez, 2000, Tondu, 2012]. Although FAMs are traditionally pneumatically activated, the use of hydraulic artificial muscles may greatly improve the overall system efficiency, in comparison to pneumatic FAMs [Tiwari et al., 2012]. Hydraulic FAMs have therefore been the subject of a variety of recent studies [Meller et al., 2014, Kothera

et al., 2009, Chapman and Bryant, 2018, Focchi et al., 2010].

Hydraulic FAMs, also known as hydraulic artificial muscles (HAMs), pose a number of potential advantages compared to traditional, pneumatic FAMs. HAMs have been observed to increase pressure-force bandwidths and exhibit less sensitivity to load [Focchi et al., 2010]. Additionally, hydraulic systems can achieve greater degrees of efficiency and exhibit a quicker response time than pneumatic systems [Focchi et al., 2010, Meller et al., 2014]. For both hydraulic and pneumatic systems, mathematical models have been developed to describe the contraction force of a FAM [Tondu and Lopez, 2000, Meller et al., 2014, Chou and Hannaford, 1996, Kothera et al., 2009]. FAMs are often assumed to be thin-walled cylinders throughout their contraction [Tondu, 2012, Chou and Hannaford, 1996]. To account for inherent nonlinearities of the FAM as it deforms, including end-effects and elasticity, geometric and empirical correction factors have been introduced [Tondu and Lopez, 2000, Tondu, 2012, Meller et al., 2014].
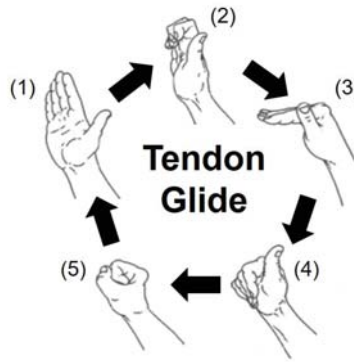
Figure 2: Tendon glide pattern of exercise. From the starting position (straight hand), there are four different hand positions- an L-shape, a hook fist, a straight fist, and a full fist- which are completed cyclically to improve or preserve a patient's range of motion. Adapted from "Open Carpal Tunnel Release Post-Op Guidelines" by UVA Hand Center.

One of the frontiers of FAM use in the human-robot interaction is rehabilitation. A number of prosthetic and orthotic devices have been developed which employ robotics [Gupta et al., 2008, Polygerinos et al., 2015, Agarwal et al., 2015, Kim and Deshpande, 2017]. The beneficial role robotic systems can play in rehabilitation following stroke, particularly for the hand and arm, has been demonstrated through clinical comparisons [Kutner et al., 2010, Volpe et al., 1999, Takahashi et al., 2008]. An important physical therapy exercise for the recovery and maintenance of hand dexterity is known as tendon glide and can be performed actively or passively [Wehbe, 1987]. Tendon glide, shown in Figure 2, is comprised of five distinct hand positions dictated by the orientation of the joints of the fingers. In position one, considered here as the starting point of the exercise, the fingers are fully extended and all joints are aligned. In order to achieve position two, the proximal interphalangeal (PIP) joint and the distal interphalangeal (DIP) joint are both flexed as much as possible to form what is called a hook fist. In order to achieve position three, the PIP and DIP joints extend and the metacarpophalangeal (MCP) joint flexes to form an L-shape. In position four, the PIP joint flexes from position three to form a straight fist. To reach position five, known as a full fist, the DIP joint flexes. The patient then starts over with position one to continue the exercise.

Robotic exoskeleton devices have the potential to improve a patient's physical therapy, particularly tendon glide, through both active and passive rehabilitation methods, while also preserving the quality of the exercise over time [Takahashi et al., 2008]. Active motion refers to the pa-

tient's participation in the movement. Passive motion refers to an outside force guiding the patient through a motion without their participation. Both classes of exercise have been clinically associated with enhanced patient recovery through the improvement of joint function and range of motion [Wolf et al., 2011, Faso and Stills, 1975, Dent, 1993, Volpe et al., 1999]. Passive tendon glide is well-suited to be implemented with a soft exoskeleton, as it consists of achieving five well-defined positions cyclically. Soft robot actuators have the potential to be used in a rehabilitation exoskeleton to achieve the positions of tendon glide. A number of soft robotic exoskeleton gloves have been proposed [Agarwal et al., 2015, Takahashi et al., 2008, Polygerinos et al., 2015, McConnell et al., 2017], but none provide a suitable actuation methodology or model for this task. The use of a soft exoskeleton actuated by hydraulically driven FAMs is therefore proposed. The advent of FAMs actuated hydraulically (rather than pneumatically) presents an opportunity to remove the bulky pressure reservoir systems that have previously driven FAM actuation in labs. By taking advantage of the relative incompressibility of hydraulic fluid, FAMs can be driven with a simple hydraulic cylinder such as a syringe. Ryu et al. [2008] introduced a haptic feedback device driven by FAMs and actuated with a small hydraulic cylinder, but their control and actuation model was empirical rather than predictive. This work establishes a method of FAM actuation capable of cycling a FAM through the positions required for a soft robotic exoskeleton to achieve the positions of tendon glide.

This work also aims to establish a control regimen capable of optimizing the motion of a FAM-actuated soft exoskeleton through the positions of tendon glide. Control of FAMs has been achieved in a variety of fashions. Several labs have employed sliding mode controllers to help overcome unmodelled aspects of the FAM's contraction [Cai, 2000, Jouppila et al., 2014, Shen, 2010, Braikia et al., 2011]. The majority of researchers employ some form of Proportional Integral Derivative (PID) control, often using neural networks or fuzzy controllers to adapt the gains of the controller to achieve the desired result [Chan et al., 2004, Anh and Ahn, 2011, Thanh and Ahn, 2006, Zhu et al., 2008, Tondu, 2014, Hesselroth et al., 1994, De Volder et al., 2011]. Nouri et al. [2002] were able to implement an adaptive controller for a FAM. Notably, all published examples of control algorithms for FAMs employ pneumatic FAMs rather than hydraulic FAMs. This work builds upon previous research in FAM control by developing and testing a linear and adaptive controller in simulation and experimentation - more specifically, a Proportional Integral (PI) controller and a Model Reference Adaptive Controller. Both controllers will actuate hydraulic FAMs. Through performance testing for three reference inputs, a step, ramp, and sinusoid, a controller will be selected based on minimal error tracking. The best performing controller will then be used with the soft exoskeleton.

This paper outlines the development of a rehabilitation exoskeleton for the hand. A novel model to describe the FAMs is introduced. The PI and MRAC controllers, which optimize the motion of the exoskeleton, are applied and evaluated. Finally, a functional exoskeleton, significant in its ability to achieve multiple hand orientations, is presented. The project is therefore threefold - the work flow and the relationship between the three components is illustrated in Figure 3.

3   Fluidic Artificial Muscle Model

A model is developed to accurately describe the FAMs used in this work. The nomenclature used to describe the models is defined. The system test bed, the construction of the FAMs, and the FAM inputs from the syringe pump are described. Next, the process by which the coupled pump-FAM model is generated, beginning with the idealized FAM model, is explained. A previously suggested cylindrico-conical FAM model [Tondu, 2012] is adapted for the coupled model and a
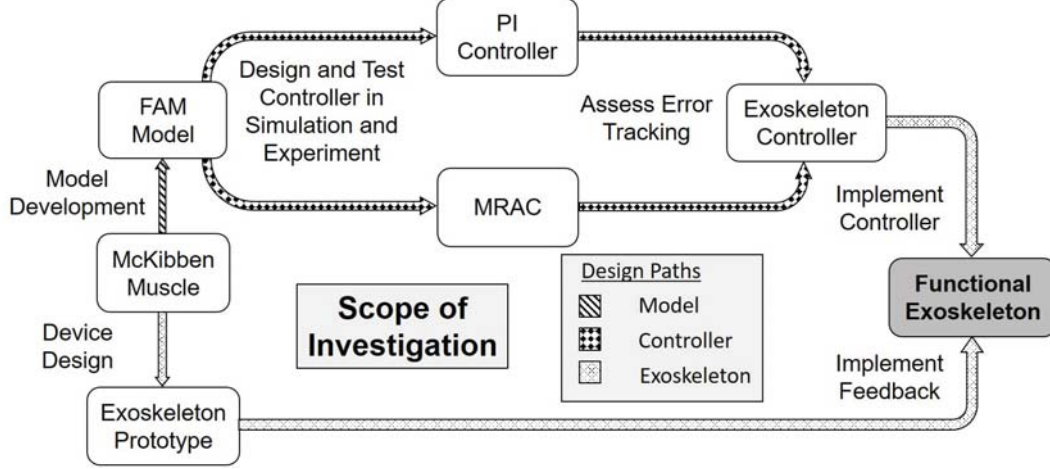
Figure 3: Scope of investigation. The investigation has three phases - modeling the FAMs, designing and testing a controller for the FAMs in simulation and experimentation, and designing the soft exoskeleton to achieve the positions of tendon glide.

novel fixed-end cylindrical model is introduced. The fixed-end model is shown to have an improved volume-strain relationship over other models for the studied system. The mathematical model is validated through the dynamic responses of the experimental setup via open loop.

3.1 Model Nomenclature

a	Geometric constant
α_0 and α	Initial and current braid angle of FAM
b	Geometric constant
d_e	Experimental displacement of cylinder
d_s	Displacement of cylinder
e_m	Model error
ε	Strain of FAM
F_m	Force applied by FAM
k_c	Constant to define cylindrical portion of FAM
l_c	Length of conical end of FAM
l_e	Length of cylindrical portion of FAM
$l_{m,0}$ and l_m	Initial and current length of FAM
l_n	Length of nonpantographic region
$l_{p,0}$ and l_p	Initial and current length of center of FAM
n	Length of displacement arrays
P_{app}	Pressure of system
r_c	Radius of cylindrical portion of FAM
$r_{m,0}$ and r_m	Radius of FAM and initial radius of FAM
r_s	Radius of hydraulic cylinder
V_c	Volume of the hydraulic cylinder
V_m	Volume of FAM
V_p	Volume required to initially fill FAM

3.2   Materials and Methods

3.2.1   Fluidic Artificial Muscle Construction

The FAMs modeled in this paper, as shown in Figure 4, are constructed from silicone tubing: the bladder, over-expanded Techflex braided cable sleeving: the outer sheath, and barbed end fittings. The FAMs are made in-house. The dimensions of the FAMs used in this paper are described in Table 1. These dimensions are selected specifically for the scale of the hand exoskeleton application. Two 54-mm FAMs can fit on the dorsal side of the hand to actuate a finger.
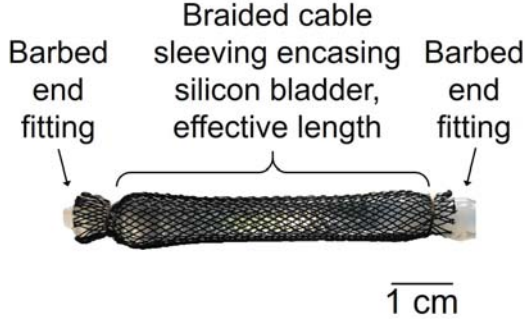
Figure 4: Fluidic artificial muscle construction. Braided cable sleeving encloses a silicon bladder. Barbed end fittings are attached to either end of the bladder and sleeving.

Table 1: Dimensions of the fluidic artificial muscles. The dimensions are selected such that the muscles could be incorporated in a hand exoskeleton.

Dimension	Measurement
Braid Angle	26.5°±1.66°
Effective Length	54.0 mm
Central Radius	4.00 mm
Bladder Inner Diameter	4.76 mm
Bladder Outer Diameter	6.35 mm
Braided Sleeving Diameter	6.35 mm

3.2.2   Piston-FAM Hydraulic System

A test bed is designed to activate a FAM using a hydraulic cylinder - in this case a syringe pump filled with water. A schematic with the hydraulic system is depicted in Figure 5. Sensors are installed to measure the strain of the FAM, displacement of the syringe pump, and pressure of the system.
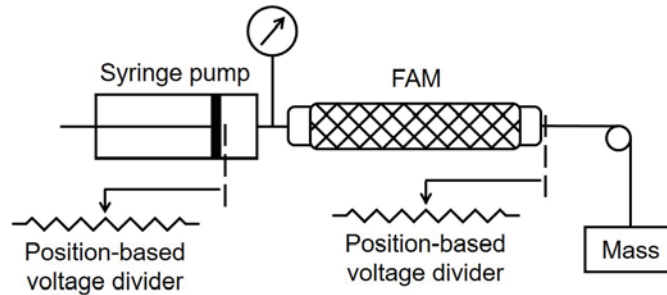
Figure 5: Schematic of the coupled hydraulic system. The position of the syringe pump, the strain of the FAM, and the gauge pressure of the system are recorded using electronic sensors. The syringe pump is driven by a threaded rod spun by a stepper motor.

The displacement of both the FAM and the syringe pump are recorded using 10 kΩ linear potentiometers (ETI Systems, California, LCP12A-50-10K), with a resolution of 1.27×10^{-5} m,

under fixed-free boundary conditions. The potentiometers are wired to determine the position of the divider. Gauge pressure is recorded using a pressure sensor (NXP Semiconductors, Netherlands, MPX2050GP) in parallel with the FAM. The pressure is transduced from the voltage across a Wheatstone bridge within the sensor, which is amplified using an instrumentation amplifier (INA118P), resulting in a resolution of 9.0×10^{-2} kPa. All data are collected using an mBed microcontroller (ARM, United Kingdom, LPC1768). Load is applied and varied through hanging masses, which ensure a constant and known load throughout the contraction of the FAM.

3.2.3 Syringe Pump for FAM Activation

A syringe pump is constructed, as shown in Figure 6, to control and measure the volumetric flow rate of the system. The plunger of the syringe is driven by the shuttle. The shuttle is threaded into a rod, which is spun by a Nema 17 stepper motor (Beauty Star, China, 17HS4401). As the threaded rod spins, the shuttle translates forward or back at a speed proportional to the angular velocity of the rod. The stepper motor is controlled by the mBed microcontroller. The displacement of the shuttle is measured using a 10 kΩ linear potentiometer.
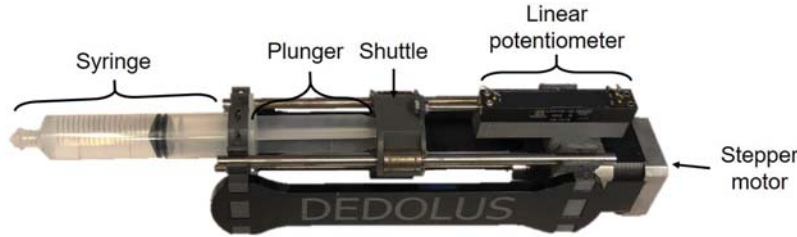
Figure 6: In-house syringe pump designed for FAM actuation. A stepper motor spins a threaded bar, which translates the shuttle and the syringe plunger. The position of the shuttle is measured using a linear potentiometer.

3.3 Piston-FAM Model Derivation and Quasi-static Validation

In order to provide a predictive model for the position of the FAM in the piston-FAM actuation system, the ideal cylindrical model, a thoroughly validated and widely used model [Tondu and Lopez, 2000, Meller et al., 2014], is first considered. The ideal cylindrical model relates the pressure, load, and strain of the FAM. The load on a FAM in a rehabilitation device would vary throughout the contraction, complicating the use of the ideal cylindrical model. However, models that are based on the volume of the FAM predict strain regardless of load, which circumvents the varying load in the exoskeleton application. As a result, a volume-based model is considered and compared to experimental data. First, the cylindrico-conical model, originally developed by Tondu [2012], is applied and found to be not fully predictive for the volume-strain relationship of the FAMs considered in this work. Tondu's model is then modified as a "fixed-end" cylindrical model, which is a novel geometric consideration of the FAMs. This section first describes the testing process. Then, the derivation and application of the ideal FAM model is discussed. The volume-based method is introduced and the two models are derived. Finally, the models are compared to experimental data to assess their validity.

3.3.1   Test Methods

Quasi-static validation testing is performed under four loads, 0.0 N, 2.93 N, 5.26 N, and 7.58 N, which are similar to the range of loads expected in the tendon glide application during rehabilitation. The FAM is cycled through three full contractions under each of the loads at a volumetric flow rate of approximately 1.1×10^{-3} mL/min. The pressure of the system, the displacement of the syringe pump, and the strain of the FAM are recorded. The starting point for the stroke of the FAM is the unloaded resting length, in this case 54 mm. The deformation of the FAM is measured using Cauchy, or engineering, strain. Strain is calculated as the ratio of the change of length of the FAM to the original length of the FAM. The volume ejected from the pump is calculated using the cross-sectional area of the syringe and the displacement of the plunger, which is measured. The displacement of the syringe is defined as the distance from the position where the first deflection of the FAM occurred. Data is sampled at a frequency of approximately 0.2 Hz.

3.3.2   Ideal FAM Model

In order to model the strain of a FAM as a function of load and pressure as was done by Tondu and Lopez [2000], the virtual work principle is first identified as,

$$F_m \, dl_m = -P_{app} \, dV_m, \tag{1}$$

where F_m is the force applied by the FAM, P_{app} is the applied pressure, dl_m is the change in length of the FAM, and dV_m is the change in volume of the FAM. The FAM is assumed to remain perfectly cylindrical and to expand according to the pantographic opening principle [Tondu and Lopez, 2000] such that,

$$\frac{l_m}{l_{m,0}} = \frac{\cos\alpha}{\cos\alpha_0} \quad \text{and} \quad \frac{r_m}{r_{m,0}} = \frac{\sin\alpha}{\sin\alpha_0}, \tag{2}$$

where $l_{m,0}$ and l_m are the initial length and current length, $r_{m,0}$ and r_m are the initial radius and current radius, and α_0 and α are the initial and current braid angle of the FAM, respectively. The pantographic opening principle is illustrated in Figure 7, which shows the opening of braids and the
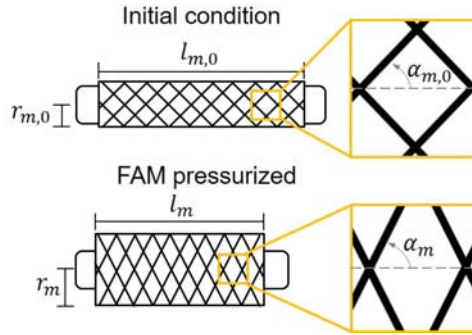
Figure 7: Representation of Ideal FAM. As the length of the FAM decreases, both the radius and the braid angle increase. The length is related to the radius through the braid angle.

resultant change in braid angle. Additionally, the variables used to describe the FAM are labeled. Combining the two equations in eqn. (2) through trigonometric substitution yields the radius of the FAM defined as a function of FAM length,

$$r_m = \frac{r_{m,0}}{\sin\alpha_0} \sqrt{1 - \left(\frac{l_m}{l_{m,0}}\right)^2 \cos^2\alpha_0}. \tag{3}$$

The strain of the FAM is defined as $\varepsilon = \dfrac{l_{m,0} - l_m}{l_{m,0}}$. Through substitution into the equation for the volume of a cylinder, the volume of the FAM, V_m, is defined as,

$$V_m = \pi r_{m,0}^2 l_{m,0} \left(\frac{(1-\varepsilon)}{\sin^2\alpha_0} - \frac{(1-\varepsilon)^3}{\tan^2\alpha_0} \right).$$

(4)

Applying the ideal cylindrical definition of FAM volume, eqn. (4), to the virtual work principle, eqn. (1), yields the force applied by the FAM defined as,

$$F_m = \pi r_{m,0}^2 P_{app} \left(a\,(1-\varepsilon)^2 - b \right),$$

(5)

where a and b are geometric constants defined as $a = 3/\tan^2\alpha_0$ and $b = 1/\sin^2\alpha_0$.
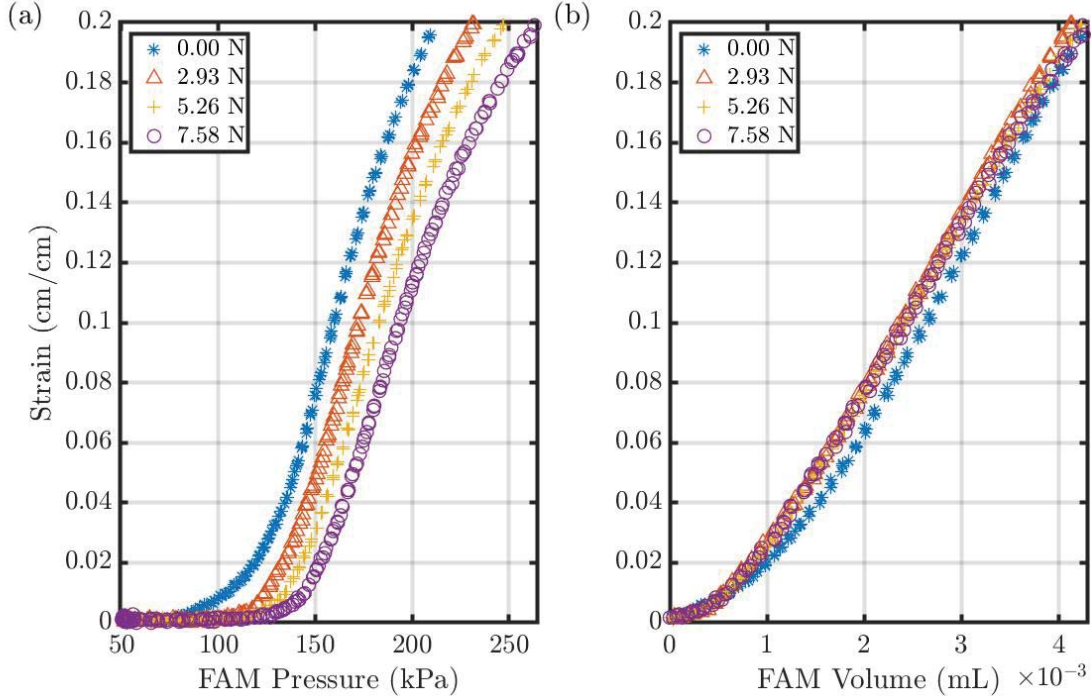
Figure 8: (a) Relationship between the pressure of the system, the force applied to the system, and the strain of the FAM. (b) Relationship between the volume transferred to the FAM, the force applied to the system, and the strain of the FAM. Throughout the FAM stroke, the pressure required to reach a contraction increases as the load increases. No such effect is observed for the relationship between the volume and the load.

The resultant model, due in part to the end-effects of the FAM, tends to overpredict the strain of the system [Meller et al., 2014], which has lead to the development of empirical correction factors [Tondu and Lopez, 2000, Meller et al., 2014]. In order to predict the strain of the FAM, both the load of the system and the pressure of the system must be known, as eqn. (5) demonstrates. The variance seen between these three variables is shown in Figure 8(a). However, because the geometry of the FAM remains constant regardless of the load, the volume of the FAM can be used to predict the strain of the FAM irrespective of load, as shown in 8(b).

3.3.3   Tondu Cylindrico-conical Model

The Tondu cylindrico-conical FAM model describes the volume of a FAM as a cylinder with two symmetric, conical frustums on either end, as depicted in Figure 9. The length of the conical ends is defined as,

$$l_c = \varepsilon l_{m,0} k_c, \tag{6}$$

where l_c is the length of the one conical end, and k_c is any constant greater than 0, such that $k_c \leq \dfrac{1 - \varepsilon_{max}}{2\varepsilon_{max}}$ [Tondu, 2012]. The total volume of both conical ends is therefore,

$$V_c = \frac{2\pi l_c}{3}\left(r_m + r_{m,0}\right)^2, \tag{7}$$

where V_c is the volume of both frustums.
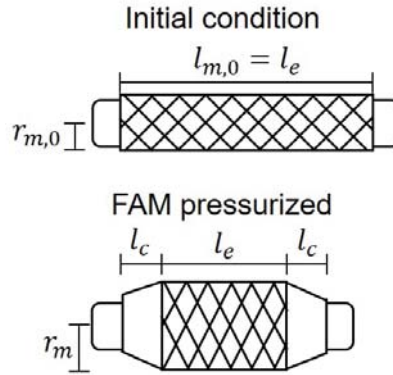
Figure 9: Tondu cylindrico-conical FAM. As the length of the FAM decreases, the radius of the cylindrical portion increases. The larger radius of the cones is determined by the current radius of the center. The height of the cones is determined as a function of the strain of the FAM.

The pantographic opening principle, as shown in eqn. (2), is applied to the cylindrical portion of the muscle with length, l_e. The cylindrical portion of the muscle is defined as, $l_e = l_m - 2l_c$. The total volume of the FAM is then defined as $V_m = V_c + V_e$, where V_e is the volume of the cylindrical portion. The virtual work theorem can again be applied to this model, as was done by Tondu [2012], resulting in,

$$F_m = \pi r_{m,0}^2 P_{app}\left(-1 + \frac{2(1-\varepsilon)}{\tan^2\alpha_0}\left(1 - \varepsilon + \frac{k_c\varepsilon(\sin\alpha_0)}{3\sqrt{1-(1-\varepsilon)^2\cos^2\alpha_0}} - \frac{4k_c\varepsilon}{3}\right)\right). \tag{8}$$

The cylindrico-conical model as described by Tondu [2012] is adapted to predict the strain of a FAM as a function of the displacement of a hydraulic cylinder, rather than as a function of load and applied pressure as in eqn. (8). The volume ejected from a hydraulic cylinder, ΔV_d is defined as,

$$\Delta V_d = \pi r_s^2 d_s, \tag{9}$$

where r_s is the internal radius of hydraulic cylinder and d_s is the displacement of the plunger of the cylinder.

The change in volume of the FAM is defined as,

$$\Delta V_m = \pi r_m^2 l_e + \frac{2\pi l_c}{3}\left(r_m + r_{m,0}\right)^2 - \pi r_{m,0}^2 l_{m,0} + V_p, \tag{10}$$

where ΔV_m is the change in volume of the FAM and V_p is the initial volume of the fluid required to completely fill the FAM, as was done by Meller et al. [2014].

Assuming a closed hydraulic system, ΔV_m can be equated to ΔV_c such that

$$\pi r_s^2 d_s = \pi r_m^2 l_e + \frac{2\pi l_c}{3}\left(r_m + r_{m,0}\right)^2 - \pi r_{m,0}^2 l_{m,0} + V_p. \tag{11}$$

The resultant model is one way of relating the displacement of a hydraulic cylinder to the strain of a FAM. However, as shown in Figure 10, it fails to accurately predict the strain of the FAMs used in this paper. For this model, $k_c = 0.5$, as it most closely matches the experimental results. The data shown is for the middle load tested, 5.26 N, and is representative of the other loads tested. Data for all the loads can be seen in the Supplemental material section in Figure S1. As the model overpredicts the strain of the FAMs made for a rehabilitation exoskeleton, a "fixed-end" cylindrical model is introduced.
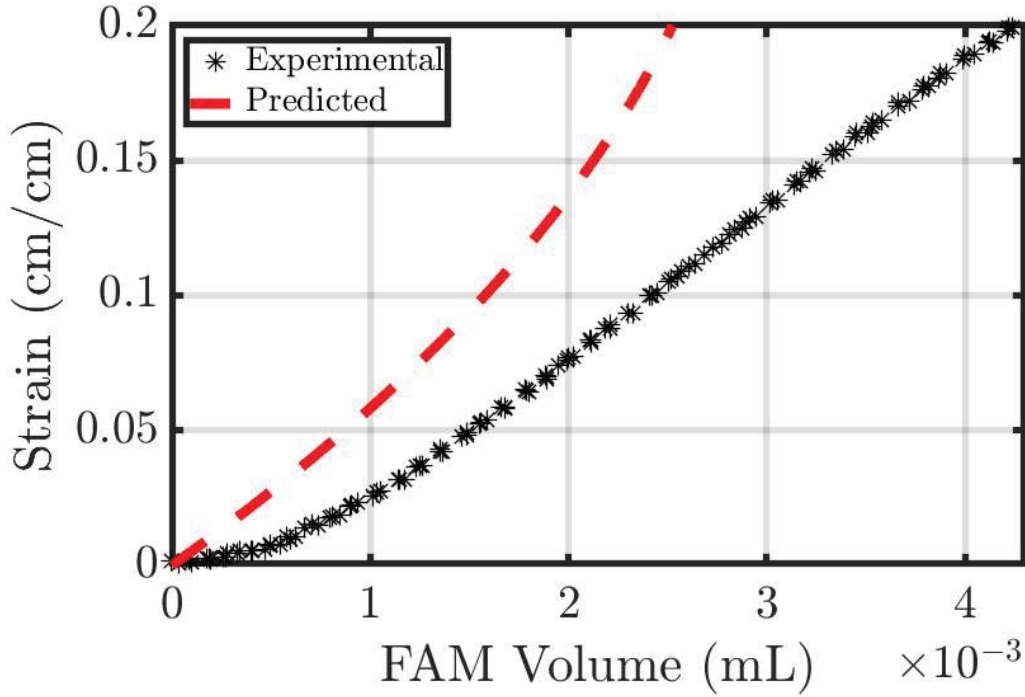
Figure 10: Discrepancy between adapted Tondu cylindrico-conical model and experimental data for a representative load of 5.26 N. The cylindrico-conical model overpredicts the strain of the FAM for a given volume.

3.3.4 Fixed-end Cylindrical Model

The adaptation of the Tondu cylindrico-conical model discussed in the previous section attempts to relate the volume of the FAM to the strain of the FAM. However, due to the relatively small

bladder diameter and low strand-count of the braided mesh used, the Tondu cylindrico-conical model does not accurately predict the contraction of FAMs in this study. To better represent the position of the FAMs with respect to volume, a modified, fixed-end cylindrical model is introduced. As was originally observed by Kothera et al. [2009], the end-effects of the FAM make it useful to consider the modeled length of the FAM as shorter than the actual length. The novel fixed-end cylindrical model combines the approaches of Kothera et al. [2009] and Tondu [2012]. In the fixed-end cylindrical model, the extremities of the FAM expand radially without contracting axially. The ends therefore consume volume without contributing to strain. As in the Tondu cylidrico-conical model, only the center portion of the FAM is considered to contract according to the pantographic opening principle. A labeled diagram of the contraction of the FAM according to the fixed-end model is shown in Figure 11. The length of the ends, l_n, is treated as a constant where, $l_n = 2.5 r_{m,0}$.
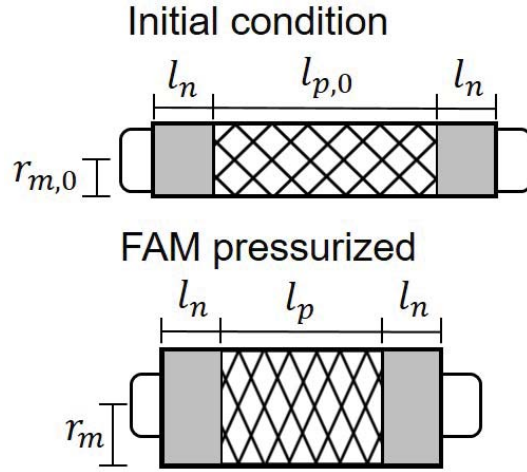
Figure 11: Fixed-end FAM. The length of the ends is constant. The radius of the FAM is determined by the length of the center portion. The volume is determined by the radius and total length, including the ends.

The length of the center region, l_p, is therefore, $l_p = l_m - 2l_n$. As only the central length, l_p, affects the radius of the FAM, r_m is redefined as a function of l_p. The relationship yields,

$$r_m = \frac{r_{m,0}}{\sin\alpha_0}\sqrt{1 - \left(\frac{l_p}{l_{p,0}}\right)^2 \cos^2\alpha_0},$$
(12)

where $l_{p,0}$ is the initial length of the pantographic region, given by $l_{p,0} = l_{m,0} - 2l_n$. The FAM is then assumed to remain cylindrical throughout its contraction. The radius of the cylinder is given by eqn. (12), which defines the radius of the center of the FAM, and the length of the cylinder is the total length of the FAM, l_m.

The volume of the FAM described in eqn. (4) is reformulated as,

$$V_m = \pi r_{m,0}^2 l_{m,0}\left(\frac{(1-\varepsilon)}{\sin^2\alpha_0} - \frac{(1-\varepsilon)}{\tan^2\alpha_0}\left(\frac{l_{m,0}(1-\varepsilon) - 5r_{m,0}}{l_{m,0} - 5r_{m,0}}\right)^2\right).$$
(13)

Consequently, the change in volume of a FAM is related to the displacement of a coupled hydraulic

cylinder by,

$$\pi r_s^2 d_s = V_p - \pi r_{m,0}^2 l_{m,0} + \pi r_{m,0}^2 l_{m,0} \left(\frac{(1-\varepsilon)}{\sin^2 \alpha_0} - \frac{(1-\varepsilon)}{\tan^2 \alpha_0} \left(\frac{l_{m,0}(1-\varepsilon) - 5 r_{m,0}}{l_{m,0} - 5 r_{m,0}} \right) \right). \tag{14}$$

The predicted strain and the experimental strain are plotted as a function of the transferred volume. The result is shown in Figure 12. Again, the data shown is for a representative load of 5.26 N. Data for all the loads is shown in Figure S2 in the Supplemental Material section. By assuming only the central portion of the FAM acts as a pantograph, the model accurately predicts the strain of a FAM as shown in Figure 12.
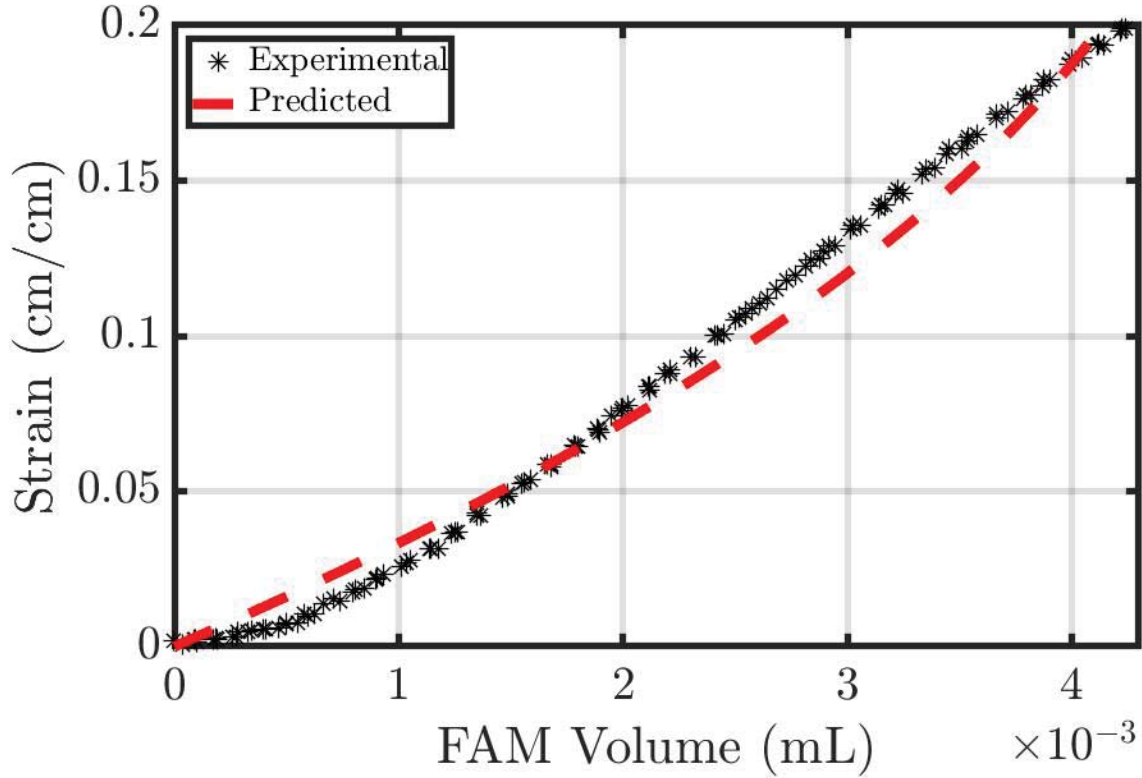
Figure 12: Validation of fixed-end cylindrical model for a representative load of 5.26 N. There is less than 0.02 strain error between the experimental and predicted contractions from 0.0 to 0.2 strain.

3.3.5 Model Comparison

The Tondu cylindrico-conical model and the fixed-end model both relate the volume ejected from cylinder via the displacement of a cylinder. The Tondu model in this case overpredicts the strain of the FAM for a given volume. The overprediction may be attributed to the magnified end-effects of small-sized FAMs, which limit the applicability of the pantographic opening principle to a smaller region. Moreover, the ends of the FAMs are approximated as frustums in the Tondu model, although visual inspection of the FAMs used in this paper reveals the ends are more cylindrical than conical when the muscle is pressurized. The fixed-end model, which assumes cylindrical end-effects, is able
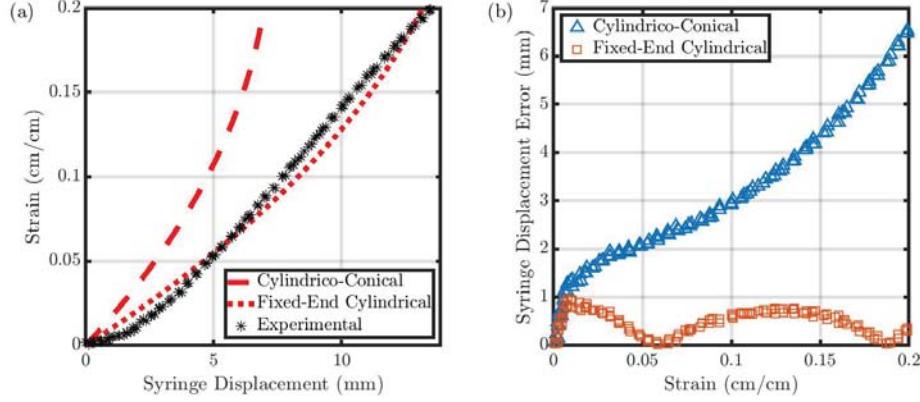
Figure 13: (a) Comparison of cylindrico-conical and fixed-end model. (b) Error of the two models. The models are both plotted as a function of syringe displacement. The fixed-end model more accurately predicts the strain of the FAM.

to more accurately predict the strain of a FAM given the displacement of a syringe pump, as seen in Figure 13(a).

The error seen in Figure 13(b) is defined as,

$$e_m = \mid d_s - d_e \mid, \tag{15}$$

where e_m is the error between the modeled syringe displacement, d_s, and the experimental syringe displacement, d_e, for a given strain. The mean of the error is defined as,

$$\bar{e}_m = \frac{\Sigma e_m}{n}, \tag{16}$$

where n is the length of the displacement arrays. The average error for the Tondu cylindrico-conical model is 3.43 mm, while the average error of the fixed-end cylindrical model is just 0.50 mm.

3.4   Dynamic Experimental Validation

In order to assess the ability of the coupled piston-FAM system to actuate FAMs dynamically and to evaluate the performance of the fixed-end model under dynamic conditions, a series of open-loop, dynamic tests are conducted and compared to model predictions. In this section, the dynamic test procedure is explained. Then, the performance of the quasi-static model in dynamics conditions is discussed. The model is scaled to account for the differences between dynamic and quasi-static testing. Finally, the scaled model is validated against further dynamic data.

3.4.1   Dynamic Testing Procedure

In order to observe the differences between quasi-static and dynamic actuation, the FAM is driven to three different strains, 0.20, 0.15, and 0.10, at three different syringe pump speeds for each, 7.4, 4.5, and 2.8 cm/min. The syringe pump used in quasi-static testing is again used in dynamic testing. Additionally, the FAMs are configured in the same set up with the same sensors. The displacement of the syringe is defined as the distance from the position where the first deflection of the FAM occurred. Dynamic testing is done under one load, 2.57 N, which is chosen arbitrarily from the previously tested loads. The FAM holds the contracted position for five seconds. The muscle then expands at the same rate at which it contracted. The cycle is meant to mimic the performance of tendon glide.

16

3.4.2 Dynamic Results

Figure 14: (a) Input of approximately 2.8 cm/min to model and experimental system for dynamic testing. (b) Strain of model and experimental system for amplitude of 0.20 strain. The simulated and experimental input of the system match well. The model is able to replicate the shape of the experimental results without lag. However, the model underpredicts the strain of the FAM throughout the contraction.

For the largest stroke of 0.20 strain, the system and the model have very similar input, yet the model underpredicts the strain significantly throughout the stroke, as shown in Figure 14. The experimental input does, however, degrade slightly at the far end of the stroke, rather than hold its plateau. The degradation is due to the syringe pump slipping, as it does not actively hold its position when stopped. The dynamic conditions clearly have an effect on the relationship between the strain and the volume of the FAM. The difference between the dynamic and quasi-static response could arise from friction. Given that the movement of the braided sheath surrounding the FAM largely determines the shape of the FAM, the interweave friction that Tondu [2012] discusses could affect the shape of the FAM. In quasi-static testing, the friction is static and likely greater than the dynamic friction that would be expected during dynamic testing. Less friction may allow the braids to open more freely, causing the muscle to shorten more with the same volume when compared to higher friction scenarios. With the possible effects of friction in mind, the model is scaled linearly by a factor of 1.35, which is determined empirically, leading to much better prediction as shown in Figure 15. The same scaled model is expanded to varied rates for the same amplitude, as well as two other amplitudes.
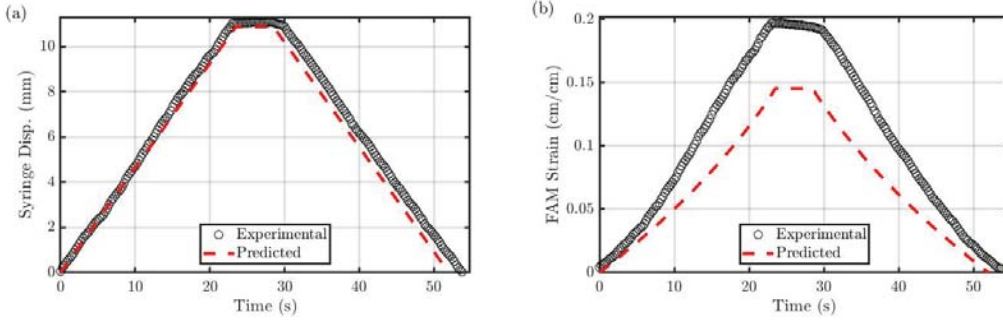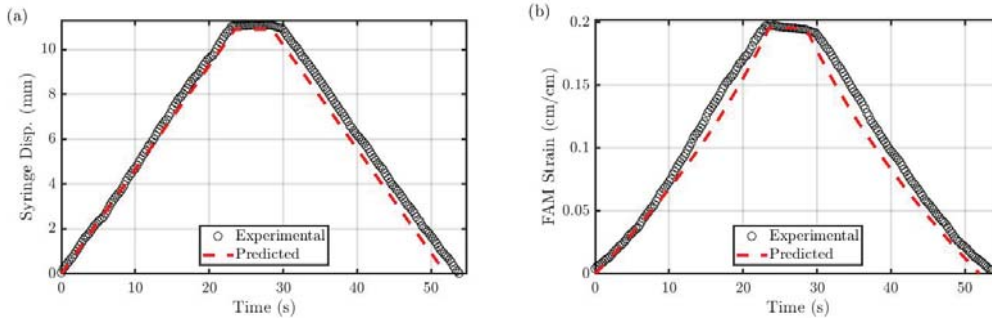

Figure 15: (a) Input of approximately 2.8 cm/min to model and experimental system for dynamic testing. (b) Strain of scaled model and experimental system for amplitude of 0.20 strain. After adjusting for the effects of dynamic versus static friction, the model accurately predicts the experimental strain.
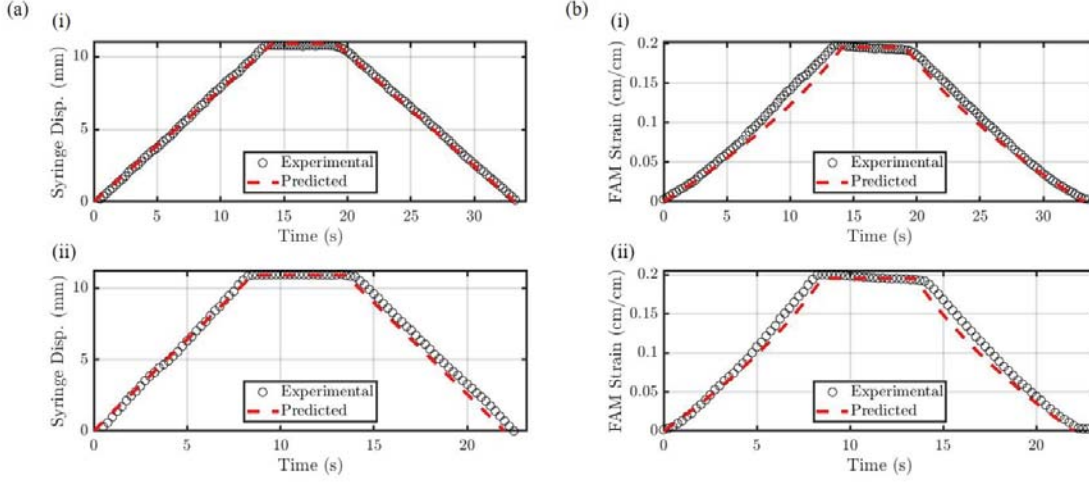
Figure 16: (a) Input to model and experimental system for dynamic testing: (i) 4.5 cm/min (ii) 2.6 cm/min. (b) Strain of scaled model and experimental system for amplitude of 0.20 strain. After adjusting for the effects of dynamic versus static friction, the model accurately predicts the experimental strain.

The scaled model reasonably predicts the contraction of the FAM for all amplitudes and loads, as shown in Figures 15 - 18. The scaled model least accurately predicts the strain of the FAM for
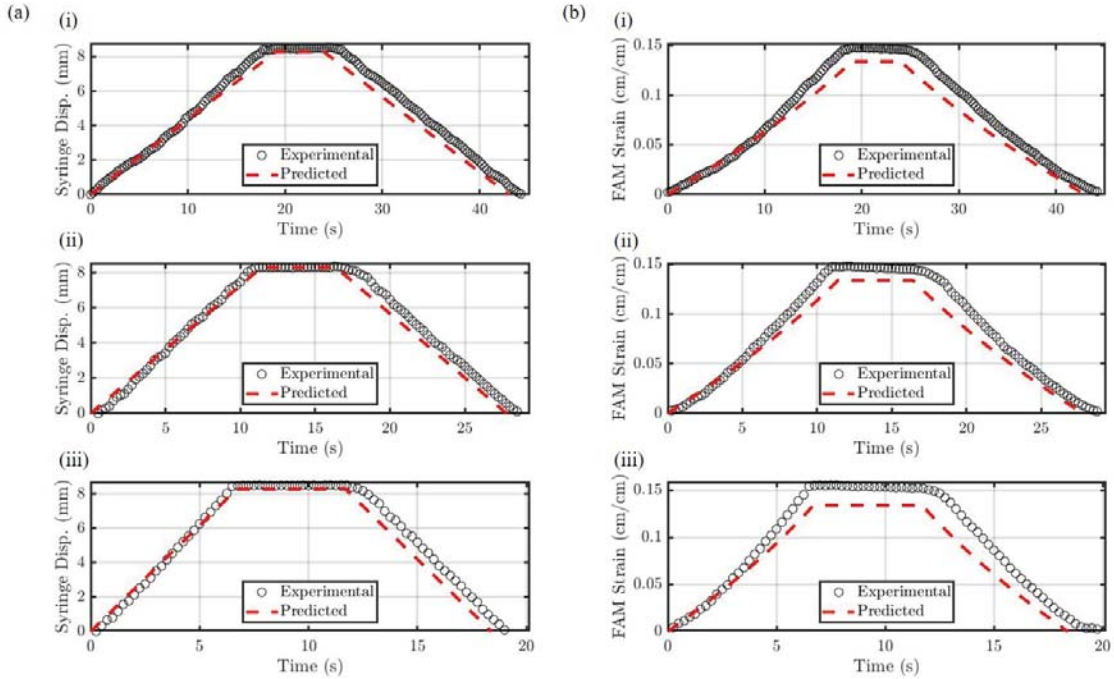
Figure 17: (a) Input to model and experimental system for dynamic testing: (i) 7.4 cm/min (ii) 4.5 cm/min (iii) 2.6 cm/min. (b) Strain of scaled model and experimental system for amplitude of 0.15 strain. After adjusting for the effects of dynamic versus static friction, the model accurately predicts the experimental strain. The discrepancy at the peaks is due in part to a slight mismatch inherent to the model.

18

the amplitude of 0.15 strain. The error for the 0.15 amplitude stroke can be attributed in part to the error seen in the fixed-end model under quasi-static conditions, which is evident in Figure 12 and 13(b). The scaled model, for all amplitudes and rates, generally underpredicts the strain of the FAM. The experimental and modeled input correspond better for the low amplitude tests shown in Figures 17(a) and 18(a). As the system is under less pressure at the lower strains, less slipping occurs while the pump idles at the peak of the contraction.

Figure 18: (a) Input to model and experimental system for dynamic testing: (i) 7.4 cm/min (ii) 4.5 cm/min (iii) 2.6 cm/min. (b) Strain of scaled model and experimental system for amplitude of 0.10 strain. After adjusting for the effects of dynamic versus static friction, the model accurately predicts the experimental strain.

3.5 Discussion

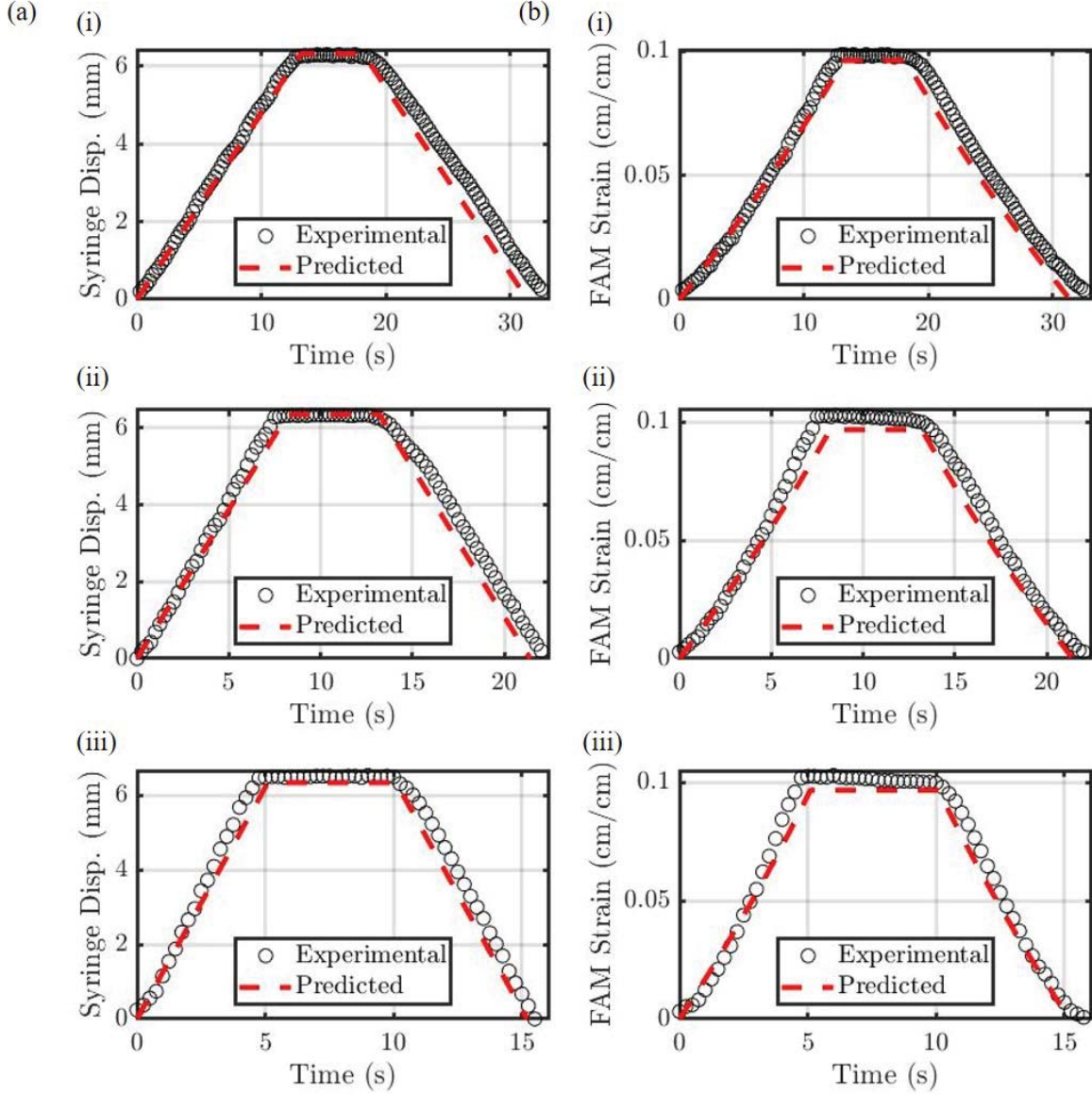This section introduces a fully coupled piston-FAM model. The novelty of the model is the ability to determine the strain of the FAM, knowing only the volume transferred to the FAM via the displacement of a hydraulic cylinder. The use of a coupled piston-FAM model eliminated the need to consider the additional pressure required to actuate a FAM under greater load, as was demonstrated by the consistent relationship between FAM strain and FAM volume shown in Figure 8(b). The pressure required to command a strain appeared to increase linearly with load, as validated in Figure 8(a). The syringe pump accounted for this increased pressure by applying more force to the plunger during contraction. By innately applying more force when required, the model was able to predict the strain of the FAM without knowledge of the load.

Since traditional models were not to be suitable for the FAMs used in this work, a novel fixed-end cylindrical model was introduced. The model built upon previous models by providing a functional way to describe the volume of small FAMs, and relate the FAM's volume and strain. The model can be tuned to fit other small FAMs by measuring the length of the fixed-ends where no appreciable contraction is occurring. In this way, the model is predictive, yet potentially compatible with a number of FAM designs.

The novel, fixed-end model was found to replicate the shape of a dynamic FAM response well, but consistently underpredict the strain. This was hypothesized to be the result of frictional differences. When the model was scaled, it was able to predict the dynamic response of a FAM with reasonable accuracy. The differences in the dynamic and quasi-static responses warrants further investigation.

By employing a coupled piston-FAM system, the traditional, bulky pressure reservoirs required to actuate traditional FAMs were eliminated. The system only required a method for actuating the plunger of the hydraulic cylinder. In other systems, this could be achieved through a number of linear actuators or rotational actuators with gearing. The size of the hydraulic cylinder could be as small as the maximum volume of the FAM. The syringe pump design, therefore, offers improved portability and utility, in comparison with the traditional, bulky tanks required to supply pressure.

Additionally, the model employs a direct relationship between the position of the FAM and the position of the hydraulic cylinder. Therefore, control can be achieved with less information about the system state. Other FAM models require both the load and pressure of the system to be known in order to predict the position of a FAM [Tondu and Lopez, 2000, Meller et al., 2014]. An exoskeleton employing FAMs actuated with a hydraulic cylinder could be used to articulate a patient's hand through the positions of tendon glide for rehabilitation with minimal hardware and sensory information to increase portability for the patient. The system would not require pressure sensors in order to control the position of the FAM, nor would the load of the system need to be known. The model proposed therefore increases the utility of FAMs in robotic applications, in particular, the area of rehabilitation robotics.

4 Linear and Adaptive Control Algorithms

To effectively control the FAMs used in this paper, a control system which governs the amount of fluid injected to the FAM is introduced. A simulation for the dynamics of the whole system, including the pump and the controller, is designed. Both a Proportional Integral (PI) controller and a Model Reference Adaptive Controller (MRAC) are implemented in simulation and experiment. The fidelity of these controllers when responding to step, ramp, and sinusoid inputs is evaluated. Ultimately, the controller best able to track the reference inputs is considered for the rehabilitation device application.

4.1   Control Nomenclature

a	System state constant
a_r	Reference system state constant
b	System state constant
b_r	Reference system state constant
d_s	Displacement of cylinder
$e_\mathrm{ad}(t)$	MRAC error
$e_\mathrm{PI}(t)$	PI error
γ_r	Adaptive tuning parameter
γ_x	Adaptive tuning parameter
k_P	Proportional gain
k_I	Integral gain
r	MRAC desired strain
t	Time
$\theta_\mathrm{r}(t)$	Adaptive gain
$\theta_\mathrm{x}(t)$	Adaptive gain
$u(t)$	Generic control effort
$u_\mathrm{ad}(t)$	MRAC control effort
$u_\mathrm{exp}(t)$	Experimental control effort
$u_\mathrm{id}(t)$	MRAC ideal control effort
$u_\mathrm{PI}(t)$	PI control effort
$u_\mathrm{sim}(t)$	Simulated control effort
σ	Standard deviation
$x(t)$	FAM strain
$x_\mathrm{d}(t)$	Desired FAM strain
$x_\mathrm{exp}(t)$	Experimental FAM strain
$x_\mathrm{m}(t)$	Measured FAM strain
$x_\mathrm{r}(t)$	Reference FAM strain
$x_\mathrm{sim}(t)$	Simulated FAM strain

4.2   Control Simulation

A Simulink block diagram is developed to simulate the system. The major components of the simulation, as labelled in Figure 19, are the FAM, the pump, and the controller, whether a PI or and MRAC. The pump is modelled as a motor where rotation results directly in fluid flow. The system is assumed to be free of the effects of static and dynamic friction. The simulation accounts for damping through a damping coefficient, which is tuned based on experimental data. The load on the pump is approximated through a linear relationship between the strain of the FAM and the torque on the motor. The FAM contracts as the pressure increases and can therefore be used to estimate the torque-load of the pump.

4.3   Control Architecture

The control algorithms described in this section are implemented through an mBed microcontroller (ARM, United Kingdom, LPC1768). Positional feedback is achieved via the linear potentiometers described in section 3.2. The mBed microcontroller updates the control effort at 100 Hz. The syringe pump described in section 3.2.3 is redesigned with a DC motor (Pololu, Nevada, 2825) rather than a stepper motor. The use of a DC motor allows for control of the pump to be achieved
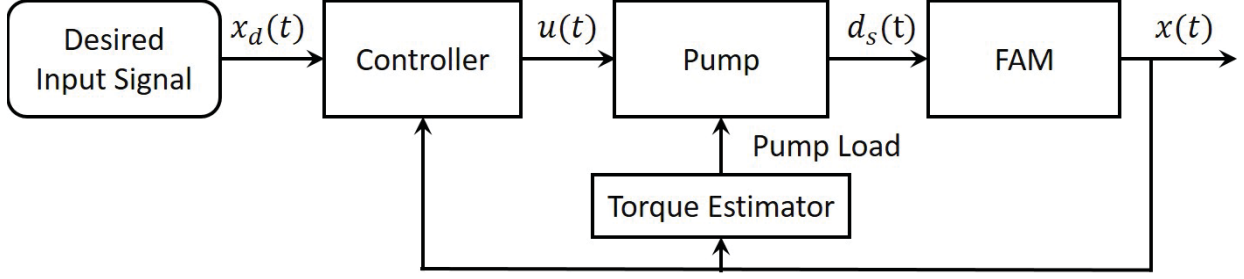
Figure 19: Illustration of Simulink model The simulation takes a desired input, $x_\mathrm{d}(t)$, determines the controller effort, $u(t)$, and uses a model of the pump to estimate the displacement of the plunger, d_s, which allows for the strain of the FAM to be estimated. The load on the pump is estimated via a proportional relationship between the strain of the FAM and the torque on the motor.

by simply varying the voltage across the motor, rather than by varying the step size. The control effort is a pulse width modulation (PWM) signal controlling the voltage applied across the DC motor. The DC motor translates the shuttle, which results in fluid flow. The control architecture is illustrated in Figure 20.
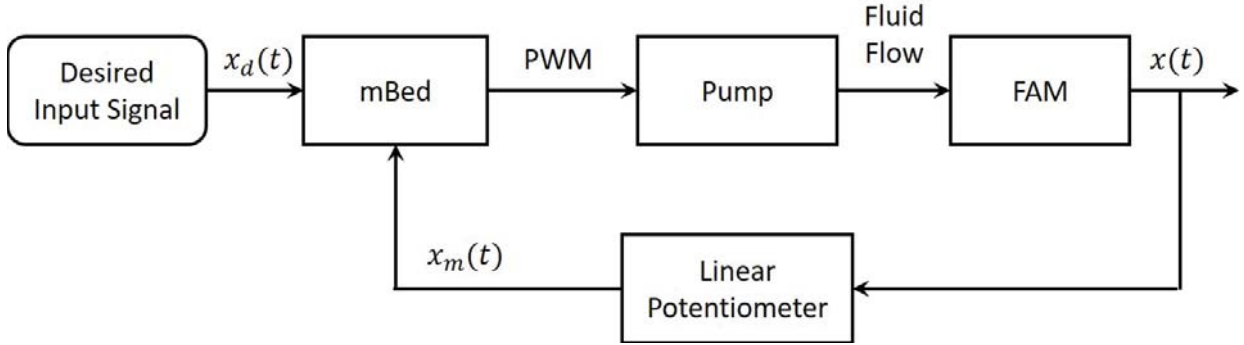
Figure 20: Block diagram of the control architecture. The mBed microcontroller calculates the control effort, sent as a PWM signal to the pump. The pump causes fluid to flow into or out of the FAM, resulting in a change in position. The position of the FAM is read by a linear potentiometer.

4.4 Control Test Methods

Both the PI controller and the MRAC are tested using the linear test bed described in section 3.2. Data is sampled at 10 Hz using an mBed microcontroller (ARM, United Kingdom, LPC1768). A step, ramp, and sinusoid is supplied as the desired input signal, $x_\mathrm{d}(t)$, for the system. 30 trials are performed for each signal and controller. Each of the signals is shown in Figure 21. The step is an instantaneous step at $t = 0.01$ from 0.0 to 0.2 strain. The ramp signal has a slope of 0.02 and a final value of 0.2 strain. The equation of the sinusoidal wave is $x_\mathrm{d}(t) = .1(1 - cos(.1\pi t))$. The period of the signal is 20 seconds in order to approximate the frequency of a typical rehabilitation exercise. The mean of each of the 30 trials is analyzed for response characteristics. The standard deviation for each signal is displayed as a shaded region on each graph. To counteract the effects of friction in experimentation, a constant voltage of 6.36 V is added to the signal produced by the

controller. The constant voltage, determined experimentally, is equivalent to the minimum voltage that enables the pump to actuate in the unloaded configuration.
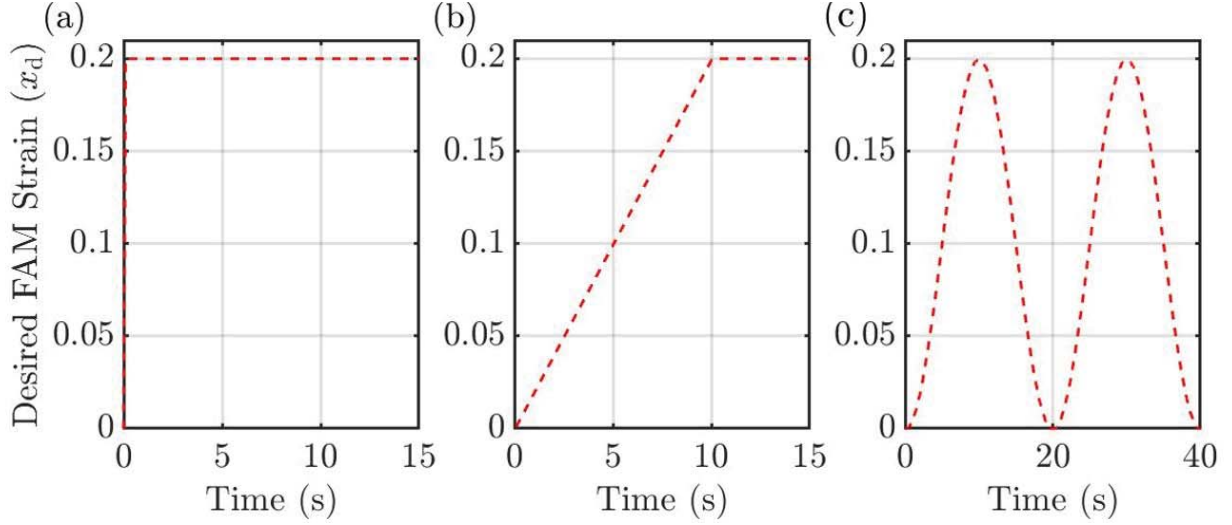
Figure 21: Desired response signals. (a) Step (b) Ramp (c) Sinusoidal. The signals are sent to the system under both PI controller and MRAC in order to gauge tracking error.

4.5 Proportional Integral Controller

4.5.1 Derivation

For the purpose of FAM actuation, a PI controller is used as described in Ogata [2009] and Dorf and Bishop [2010]. The block diagram of this controller is shown in Figure 22. In this model, the user specifies the desired strain, $x_\mathrm{d}(t)$, as the system input, which is then compared to the current measured state, $x(t)$. The system error, $e_\mathrm{PI}(t)$, is defined as follows,

$$e_\mathrm{PI}(t) = x_\mathrm{d}(t) - x(t). \tag{17}$$
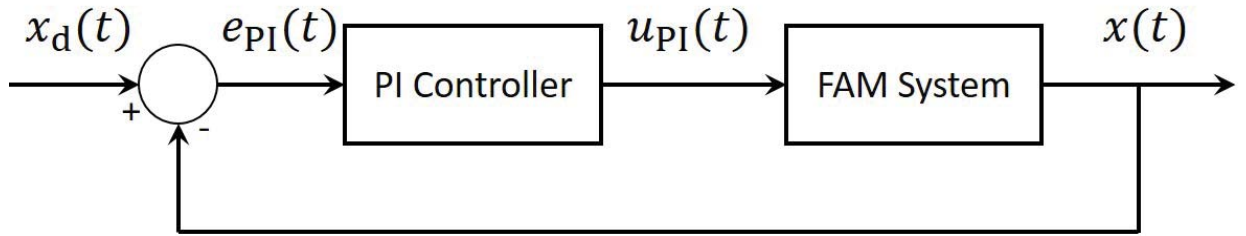
Figure 22: Block diagram of the closed-loop system using a Proportional Integral controller. For PI control, the error $e_\mathrm{PI}(t)$ is determined from the state $x(t)$ and desired state $x_\mathrm{d}(t)$. A control effort, $u_\mathrm{PI}(t)$, based on $e_\mathrm{PI}(t)$ is then input into the system.

Based on this definition of the error, the PI controller then determines the control input, $u_\mathrm{PI}(t)$, through the following law,

$$u_\mathrm{PI}(t) = k_\mathrm{P} e_\mathrm{PI}(t) + k_\mathrm{I} \int_0^t e_\mathrm{PI}(\tau)d\tau, \tag{18}$$

where k_P is the proportional gain and k_I is the integral gain to minimize steady state error.

To tune the controller, a procedure similar to the Ziegler-Nichols Critical Gain method presented in Ogata [2009] is applied. For a desired strain, $x_d(t) = 0.2$, and with the integral gain, k_I, set to 0, the proportional gain, k_P, is steadily increased until the control input, $u_{PI}(t)$, peaks at the upper saturation limit. The resultant value is considered to be the optimal proportional gain. Using this value, the k_I term is gradually increased until the system has minimal overshoot to ensure a proper transient response.

4.5.2 Results

The gains used the for PI controller in both experimentation and simulation for the step, ramp, and sinusoidal input are $k_P = 2.35$ and $k_I = 0.28$. The system successfully responded to the step input as shown in Figure 23(a). The mean shown is across 30 trials, and average standard deviation of the group is $\bar{\sigma} = 0.0028$, indicating reproducibility. The simulation lagged the experimental mean in the transient portion of the response. Similarly, the simulated control effort in Figure 23(b) lags the experimental effort. Both the simulation and the experimental system achieve the desired strain of $x_d(t) = 0.2$.
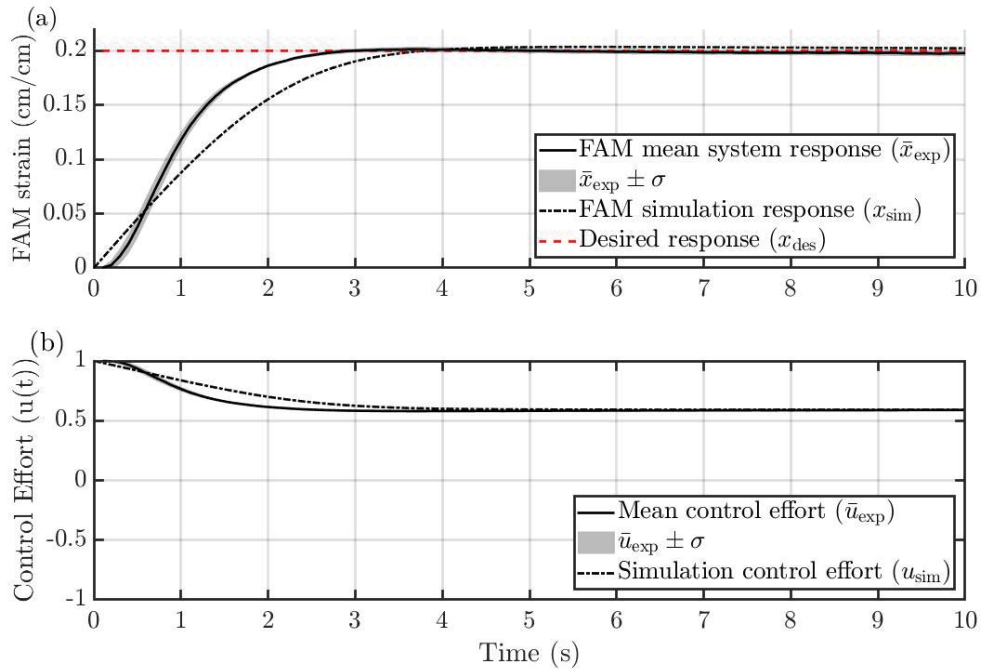
Figure 23: System response under PI control to a step input of magnitude 0.2. (a) Strain of FAM $x(t)$ (b) Control Effort $u_{ad}(t)$. The group has an average standard deviation of $\bar{\sigma} = 0.0028$. Simulation lags the experimental data in the transient portion of the response. Both the simulation and the experimental system achieve the desired strain of $x_d(t) = 0.2$.

As shown in Figure 24(a), the experimental system lagged the ramp input by approximately 0.8 seconds throughout the contraction. The system ultimately settled lower than the desired final value of $x_d(t) = 0.2$. The simulation also lagged the reference system, more so than in experimentation, but settled above 0.2. The shape of the response mirrors that of the desired response. Figure 24(b) shows remarkable similarity between the simulated and experimental control effort, $u_{PI}(t)$.
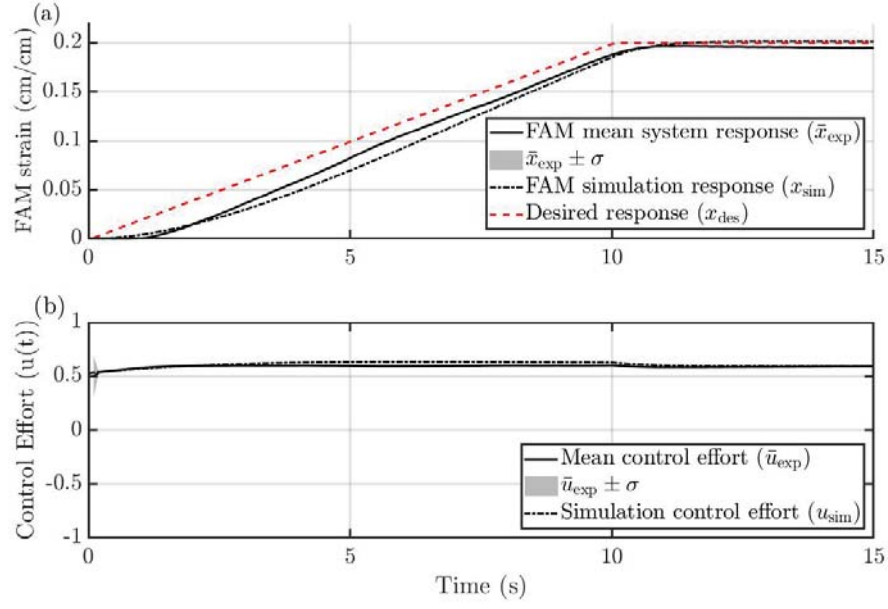
Figure 24: **System response under PI control to a ramp input of slope 0.02 with a final value of 0.2. (a) Strain of FAM** $x(t)$ **(b) Control Effort** $u_{\mathrm{ad}}(t)$**.** The group has an average standard deviation of $\bar{\sigma} = 0.0013$, indicating reproducibility. Both the simulation and the experimental strain lag the reference system by approximately 0.8 seconds. The simulated and experimental control efforts are similar.
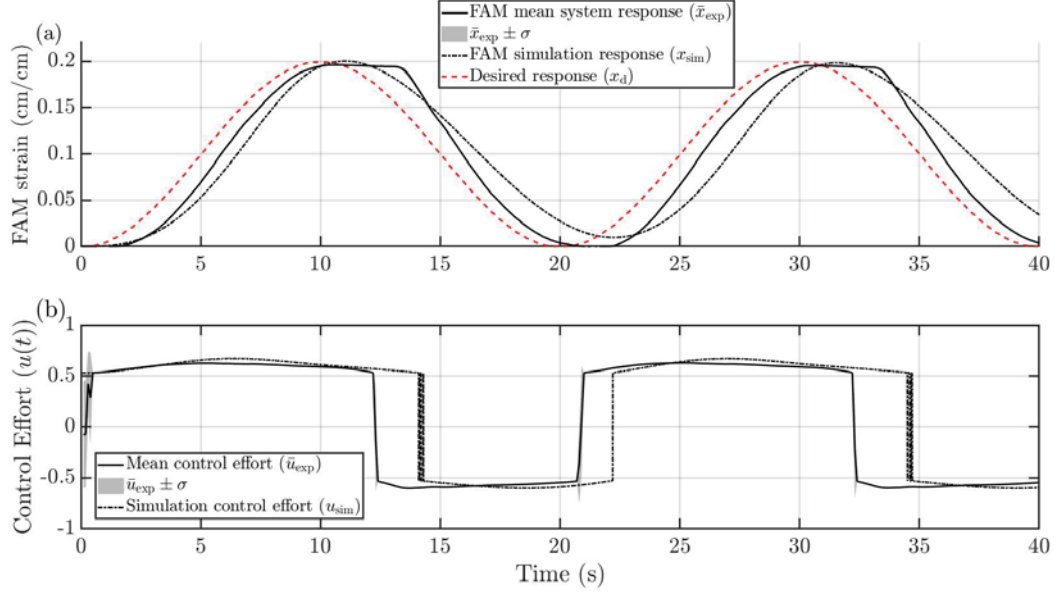
Figure 25: **System response under PI control to a sinusoidal input. (a) Strain of FAM** $x(t)$ **(b) Control Effort** $u_{\mathrm{ad}}(t)$**.** The group has an average standard deviation of $\bar{\sigma} = 0.0008$. Both the simulation and the experimental mean lag the desired response, $x_{\mathrm{d}}(t)$. The simulated and experimental control efforts are similar in shape, with the simulated effort out of phase with the experimental effort.

For the sinusoidal input, the system again lagged the desired response by approximately 0.8 seconds, as shown in Figure 25(a). The shape of the experimental response mirrors that of the desired response, with the exception of some sticking at the maximum contraction of the FAM, possibly due to the increased load on the motor and friction. In Figure 25(b), the experimental control effort corresponds to the simulated control effort, although it is out of phase with the simulation.

4.6 Model Reference Adaptive Controller

4.6.1 Derivation

In addition to the PI controller, a MRAC algorithm based on the theory presented in Ioannou and Sun [1996] and Narendra and Annasway [1989] is used. The block diagram, seen in Figure 26, shows the control effort as a function of the adaptive gains, $\theta_r(t)$ and $\theta_x(t)$, reference input, $x_r(t)$, and current state, $x(t)$. The adaptive gains, likewise, depend on the reference input, $x_r(t)$, current state, $x(t)$, and error between the unknown plant and reference system, $e_{ad}(t)$. Within Figure 26, $x_d(t)$ is the desired strain, $x_r(t)$ is the strain of the reference system, and $x(t)$ is the strain of the FAM. The following derivation was done by Jaramillo Cienfuegos et al. [2017] and is repeated here for the FAM system.
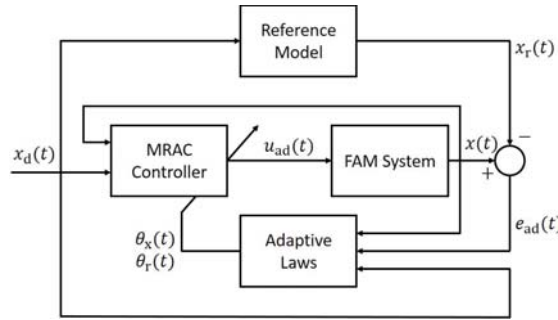
Figure 26: Block diagram of the closed loop system using a Model Reference Adaptive Controller. The error, $e_{ad}(t)$, state, $x(t)$, and desired strain, $x_{d(t)}$, are used to define the dynamics for adaptive gains, $\theta_r(t)$ and $\theta_x(t)$. The control effort is computed using these gains, which then drives the experimental system to the reference system.

The following linear structure is implemented to describe the FAM behavior,

$$\dot{x}(t) = ax(t) + bu_{ad}(t), \tag{19}$$

where $x(t) \in \mathbb{R}$ is the system state, $a \in \mathbb{R}$ is an unknown system state constant, $b > 0$ is the system input constant with known sign and unknown magnitude, and $u_{ad}(t) \in \mathbb{R}$ is the control effort. The MRAC algorithm ultimately forces the system given in eqn. (19) to converge to the following reference model,

$$\dot{x}_r(t) = a_r x_r(t) + b_r r(t), \tag{20}$$

where $x_r(t) \in \mathbb{R}$ is the reference model state, $a_r < 0$ is a negative (stable) system state constant, $b_r \in \mathbb{R}$ is a known input constant, and $r(t) \in \mathbb{R}$ is the reference input. The reference input, $r(t)$, is then chosen so that the reference system $x_r(t)$ tracks the desired trajectory, $x_d(t) \in \mathbb{R}$.

It is assumed that ideal gains, $\theta_x^* \in \mathbb{R}$ and $\theta_r^* \in \mathbb{R}$, exist to drive the system to the reference model through an ideal control law, $u_{id}(t) \triangleq \theta_x^* x(t) + \theta_r^* r(t)$. By substituting $u_{id}(t)$ into eqn. (19),

the following relationship is obtained,

$$\dot{x}(t) = (a + b\theta_x^*)x(t) + (b\theta_r^*)r(t). \tag{21}$$

The error is given by $e_{ad}(t) \triangleq x(t) - x_r(t)$. Choosing $\theta_x^* \triangleq \frac{a_r - a}{b}$ and $\theta_r^* \triangleq \frac{b_r}{b}$, the closed-loop system expression simplifies to the reference model and the error dynamics are given by

$$\dot{e}_{ad}(t) = \dot{x}(t) - \dot{x}_r(t) = a_r x(t) - b_r r(t) - (a_r x_r(t) + b_r r(t)) = a_r e_{ad}(t). \tag{22}$$

Given that the reference model is chosen to be stable ($a_r < 0$), the error dynamics are also stable, and the system state converges to the reference state. However, since a and b are unknown, the ideal gains θ_x^* and θ_r^* cannot be computed and the ideal control law $u_{id}(t)$ cannot be implemented. Hence, the ideal control law needs to be modified into an adaptive one which, instead of the ideal gains, implements adaptive gains, $\theta_x(t)$ and $\theta_r(t)$.

Theorem 1 Consider the system eqn. (19), the reference system eqn. (20) and adaptation laws given by

$$\dot{\theta}_x(t) \triangleq -\gamma_x e_{ad}(t)x(t)\text{sign}(b), \tag{23}$$
$$\dot{\theta}_r(t) \triangleq -\gamma_r e_{ad}(t)r(t)\text{sign}(b), \tag{24}$$

where $\gamma_x > 0$ and $\gamma_r > 0$ are the tuning parameters. Then, the closed-loop system given by (19), (20), (23), (24) with the adaptive control law

$$u_{ad}(t) = \theta_x(t)x(t) + \theta_r(t)r(t), \tag{25}$$

is Lyapunov stable, and the tracking error $e_{ad}(t)$ converges to zero. $\square$

Proof of Theorem 1 is explained in detail in the work of Jaramillo Cienfuegos et al. [2017].

The controller is tuned though the tuning constants γ_x and γ_r, and the reference system parameters a_r and b_r.

4.6.2 Results

The parameters used to define the MRAC are shown in Table 2. As shown in Figure 27(a), the

Table 2: Parameters defining MRAC. The parameters are the same between experiment and simulation with the exception of the initial conditions of the gains.

Parameter	Experimental	Simulation
γ_r	1000.	1000.
γ_x	900.0	900.0
$\theta_r(0)$	-7.000	2.000
$\theta_x(0)$	7.000	-2.000
a_r	-0.5000	-0.5000
b_r	0.5000	0.5000

system initially overshoots the reference trajectory significantly. The controller quickly corrects and is generally able to track the reference system, with slight oscillation. The average standard deviation of the group is $\bar{\sigma} = 0.0031$, indicating reproducibility. The control effort of the FAM,
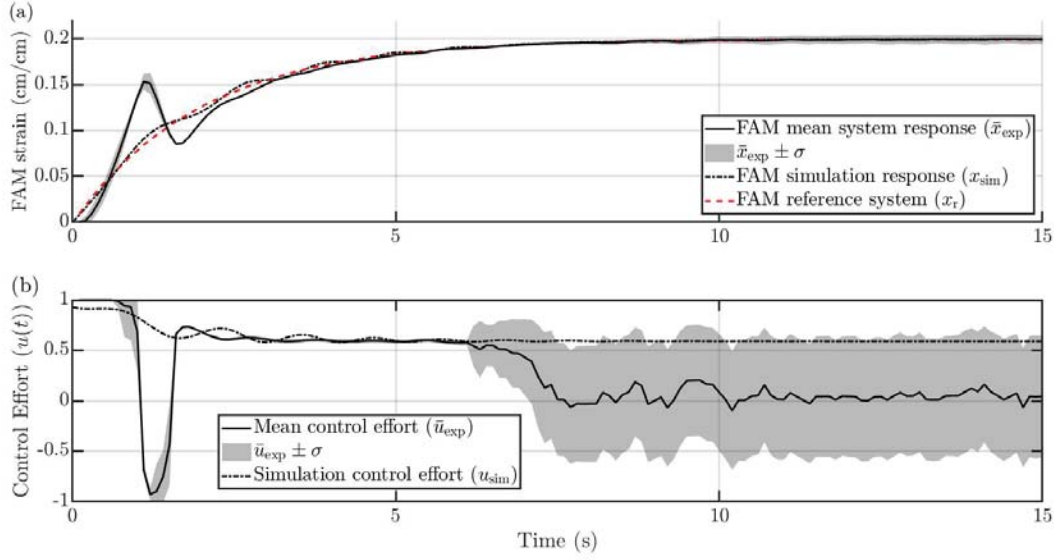
Figure 27: System response under MRAC to a step input of magnitude 0.2. (a) Strain of FAM $x(t)$ **(b) Control Effort** $u_{\mathrm{ad}}(t)$**.** The experimental and simulated strains and control efforts generally agree, with the exception of the region surrounding the strain overshoot.
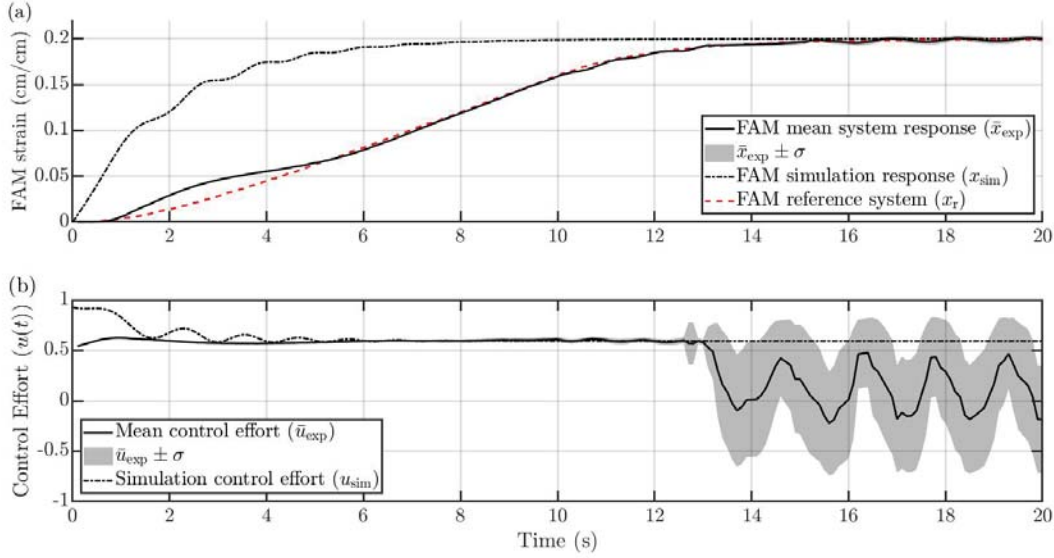
Figure 28: System response under MRAC to a ramp input of slope 0.02 with a final value of 0.2. (a) Strain of FAM $x(t)$ **(b) Control Effort** $u_{\mathrm{ad}}(t)$**.** Both the simulation and the experimental strain achieve the desired response. The simulated and experimental control efforts are similar up to $t = 13s$.

$u_{\mathrm{ad}}(t)$, is generally similar, with the exception of the large dip at $t = 1s$, as shown in Figure 27(b). The standard deviation of the control effort increases around $t = 7s$ in Figure 27(b), due to an oscillation between positive and negative control effort to maintain steady state conditions.

For the ramp case, shown in Figure 28(a), the system matched the desired response throughout

the contraction. The greatest discrepancy occurred at the beginning of the motion, exhibiting an overshoot similar to that shown in Figure 27(a), although less pronounced. The system begins to oscillate slightly as it approaches steady state at $t = 15s$. Figure 24(b) shows remarkable similarity between the simulated and experimental control effort from $t = [0\ 13]$s. A similar oscillatory behavior to that shown in 27(b) increases the standard deviation to about $\sigma = 0.5$ after $t = 13s$.

The system achieves the desired response, a sinusoidal wave, as shown in Figure 29(a). The system again exhibits overshoot at the onset of the input of the signal command, with a more more pronounced overshoot in the second period. After the overshoot, the system tracks the desired response very closely. The experimental and simulated control effort in Figure 29(b) are similar, with the experimental effort exhibiting more oscillation.
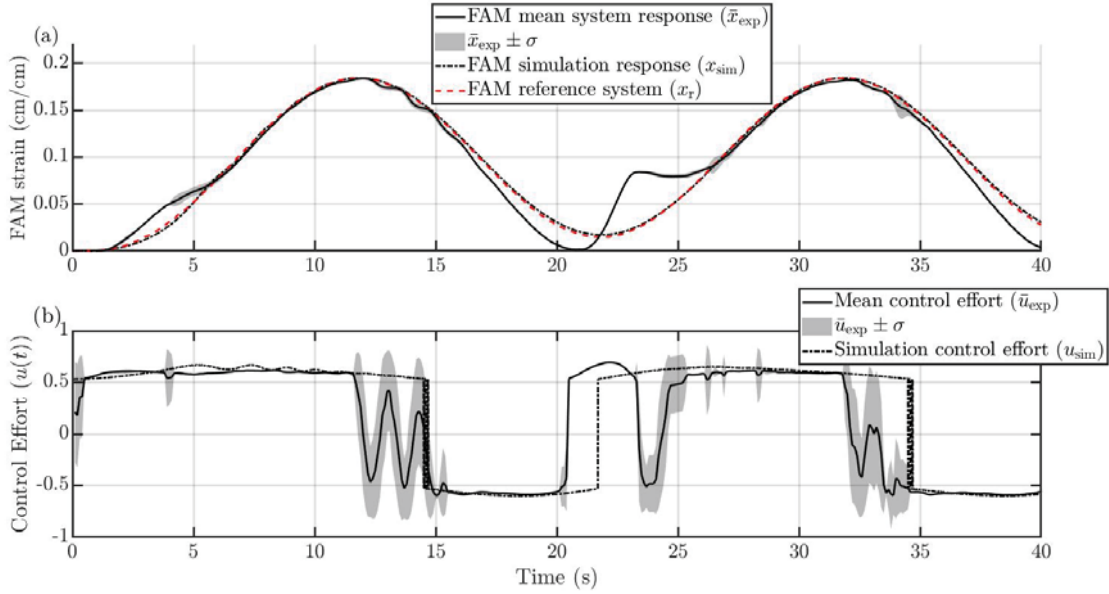
Figure 29: **System response under MRAC to a sinusoidal input. (a) Strain of FAM** $x(t)$ **(b) Control Effort** $u_{\text{ad}}(t)$**.** Both the simulation and the experimental response achieve the reference system. The simulated and experimental control efforts are similar, with the exception of some oscillation in the experimental effort.

4.7 Performance Comparison

Both the PI controller and the MRAC were successful at tracking a variety of reference signals. The MRAC, however, was more successful according to analysis of tracking error due to the persistent lag seen in the PI control. The MRAC, despite initial overshoot, was able to better track the desired signal. Side by side comparison for the step, ramp, and sinusoidal inputs are shown in Figure 30. The PI controller exhibited more tracking error, as shown in Figure 30 and Table 3. The MRAC controller, however, exhibited oscillatory behaviour. Given the intended application of a rehabilitation device, oscillations pose a safety risk, as overshoot could result in the over-bending of a joint. As the PI controller behaved without oscillation, albeit with more tracking error, the PI controller is selected for implementation in a rehabilitation device.
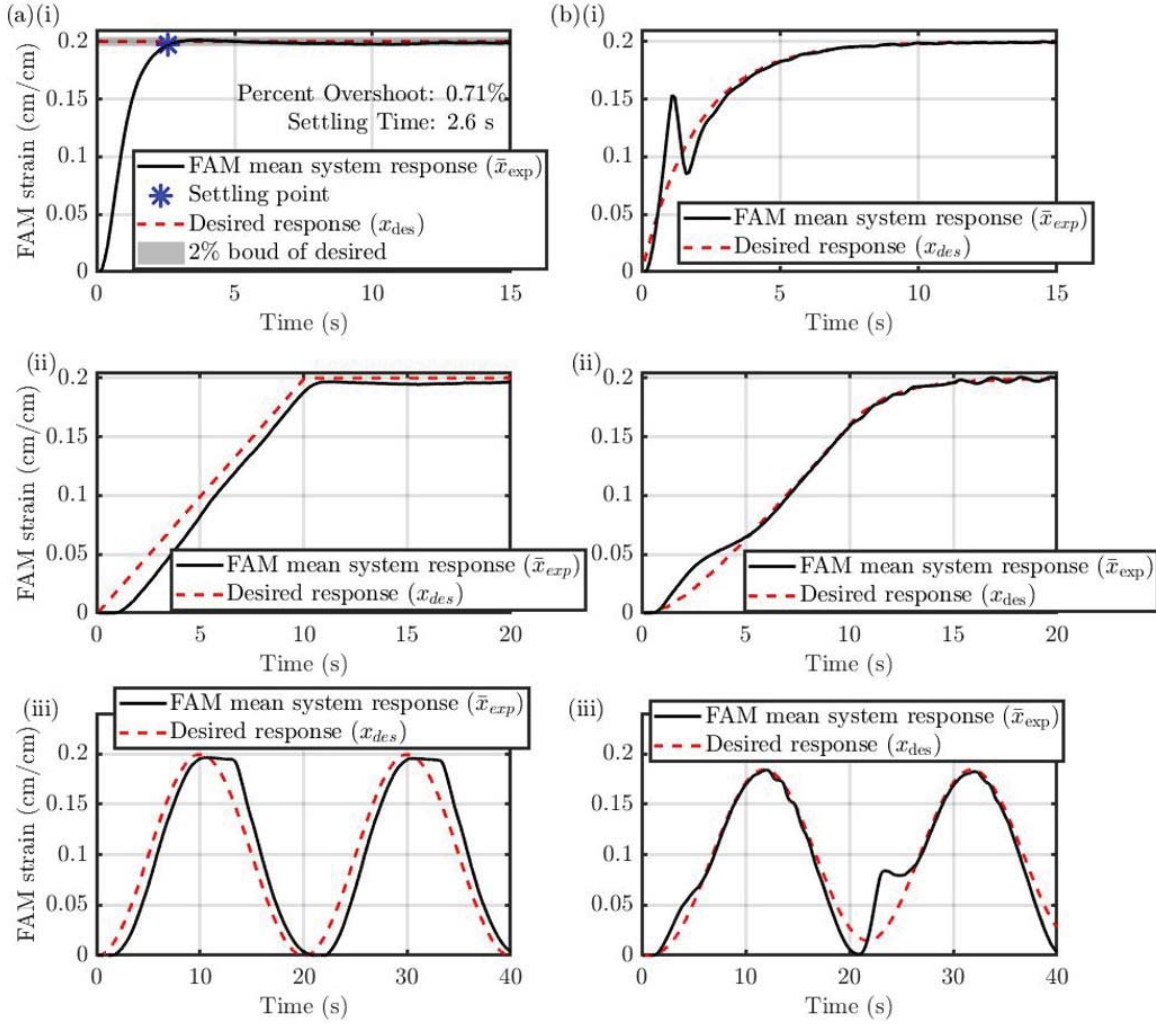
Figure 30: Absolute tracking error for each reference and controller (a) PI (b) MRAC (i) Step (ii) Ramp (iii) Sinusoidal. The PI controller lags the desired response, but imitates the shape of the reference. The MRAC exhibits oscillatory behavior, but does not lag.

Table 3: Error of System Responses. The average error of the MRAC is lower than the error of the PI controller for every reference signal.

Signal	$|\bar{e}_{PI}|$	$|\bar{e}_{ad}|$
Ramp	0.0137	0.0045
Step	0.0102	0.0034
Sinusoidal	0.0197	0.0106

5 Exoskeleton Design

To prove the feasibility of a wearable device capable of achieving the positions of tendon glide, a model finger outfitted with the components of the exoskeleton is constructed as seen in Figure 31. First, the design specifications of the finger and exoskeleton are described. Then, testing methods

and results are discussed. Finally, the design of the actual wearable device is illustrated.

5.1 Materials and Specifications

In order to achieve the positions of tendon glide, a wearable exoskeleton must be able to rotate each joint from fully flexed to fully extended. Additionally, the exoskeleton must be able to move as joints independently in order to achieve as many hand positions as possible. Furthermore, the device must be sufficiently light-weight to be worn comfortably. The model finger pictured in Figure 31 consists of three links equivalent to the phalanges, and a base equivalent to the metacarpal. The dimension of the phalanges are scaled to be anatomically representative of those of an average-sized adult male. The finger is 3D printed using a Stratasys 3D printer (Stratasys, Minnesota, Eden260VS^{TM}) and VeroClear RGD810. The exoskeleton consists of five main components: the distal plug, the proximal plug, medial hydraulic connection, the restoring force sheath, and the muscles, as described in Figure 31. Both plugs and the medial hydraulic connection are 3D printed
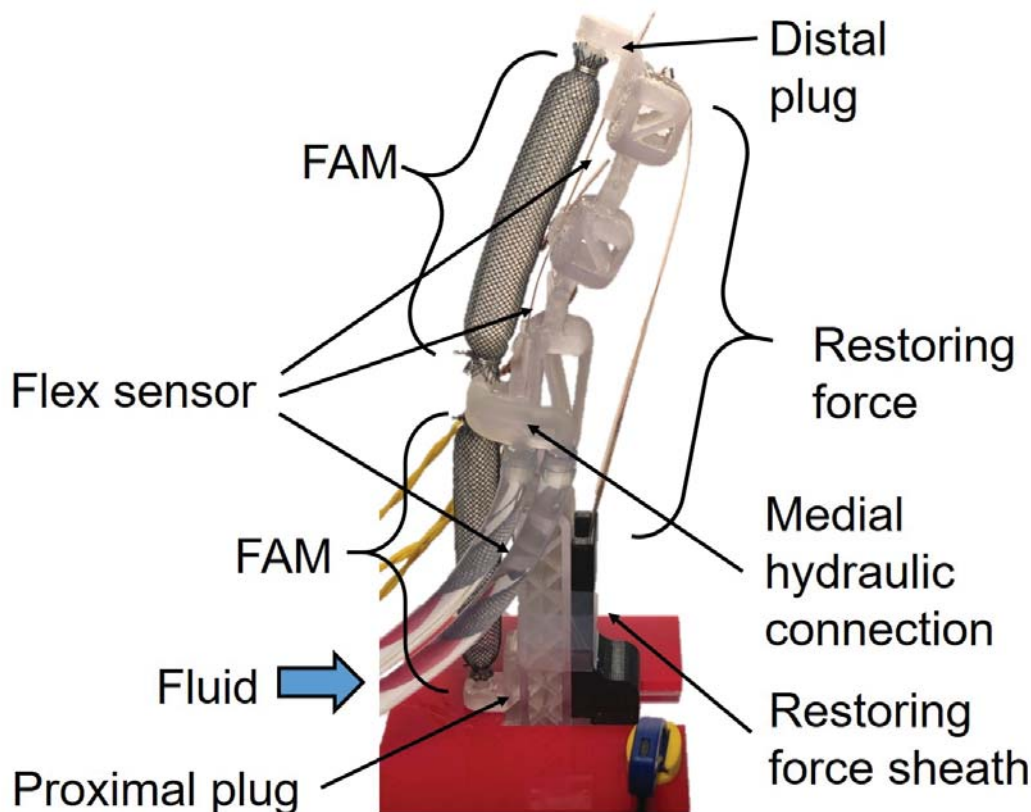
Figure 31: Finger used for testing. The finger is 3D printed and outfitted with FAMs, a restoring force, and sensors.

using VeroClear RGD810, while the restoring force sheath is 3D printed using polylactic acid (PLA). The restoring force itself is proved by a 4.58 N constant force spring (McMaster Carr, New Jersey, 9293K44) which servers as a restoring force to return the muscles to the fully extended position. The muscles are FAMs, constructed of braided sheathing and an expandable bladder, as previously discussed. The exoskeleton also features resistive flex sensors (SparkFun, Colorado, SEN-10264 ROHS) and 3D printed guides for those sensors to determine the orientation of the finger. Polyvinyl

chloride (PVC) tubing (ATP, Ohio, PVS316-516ANA) connects the medial hydraulic connection to a ball valve which allows control of each muscle individually. Pressure is supplied via the syringe pump shown in Figure 32.
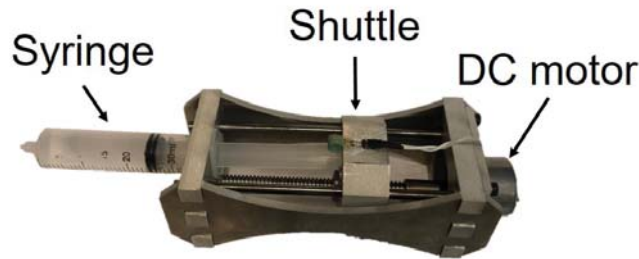
Figure 32: Pump for control testing. The DC motor drives the shuttle, which in turn depresses the syringe.

5.2 Performance Testing

Using human-in-the-loop control, the finger was able to achieve the positions of tendon glide, as shown in Figure 33. Using just two FAMs, the finger could be orientated to achieve the five hand positions required for tendon glide. The distal FAM extended the joint equivalent to the DIP prior to the PIP joint, allowing for the achievement of position (2). The achievement of position (2) was not originally sought, but discovered during testing. The maximum strain of the FAM limited the degree of extension achieved by the finger, particularly in positions (1) and (3). A single restoring force enabled the achievement of all five positions, simplifying design.
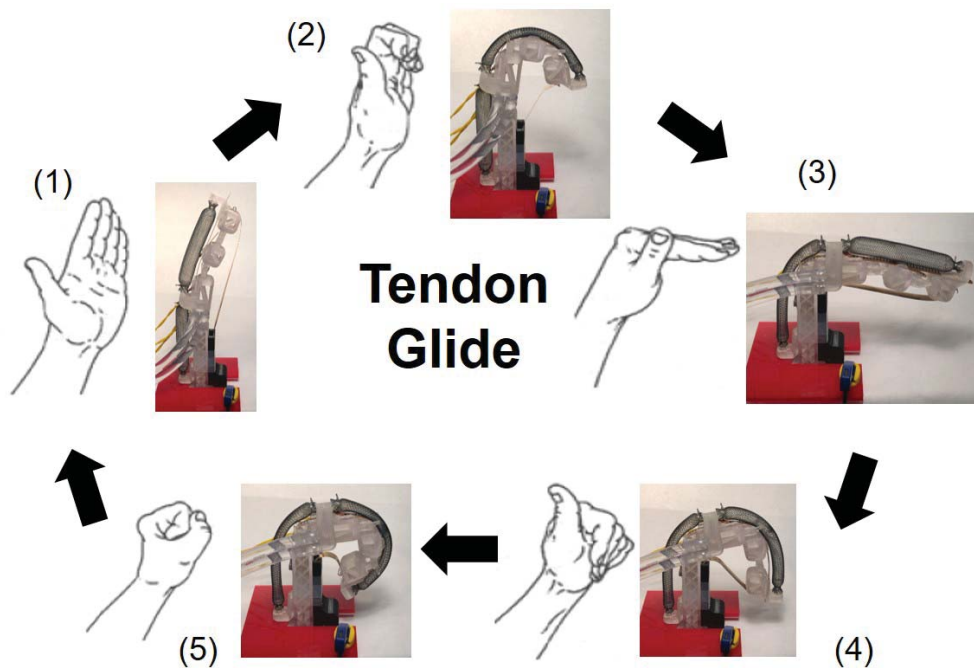
Figure 33: Test finger achieving positions of tendon glide with biological comparison. All five positions were achieved.

As previously mentioned, a PI controller is used to govern the flexion and extension of the joint. Control is applied for the distal FAM, with feedback coming from the flex sensor across the PIP joint. Figure 34 shows the mean of ten trials with a sinusoidal reference system. For the first period, the finger began from the fully relaxed position shown as position (4) in Figure 33. As the reference system flexed, the finger flexed until the PIP joint was at 90 degrees, which corresponds to position (2) in Figure 33. As the finger started with the PIP joint on the cusp of motion, there is less delay in the second period. The controller requires notably more effort when controlling the FAMs in the finger assembly, versus the linear test bed. The increased control effort is expected, given that there is a restoring force acting against the contraction of the FAMs.
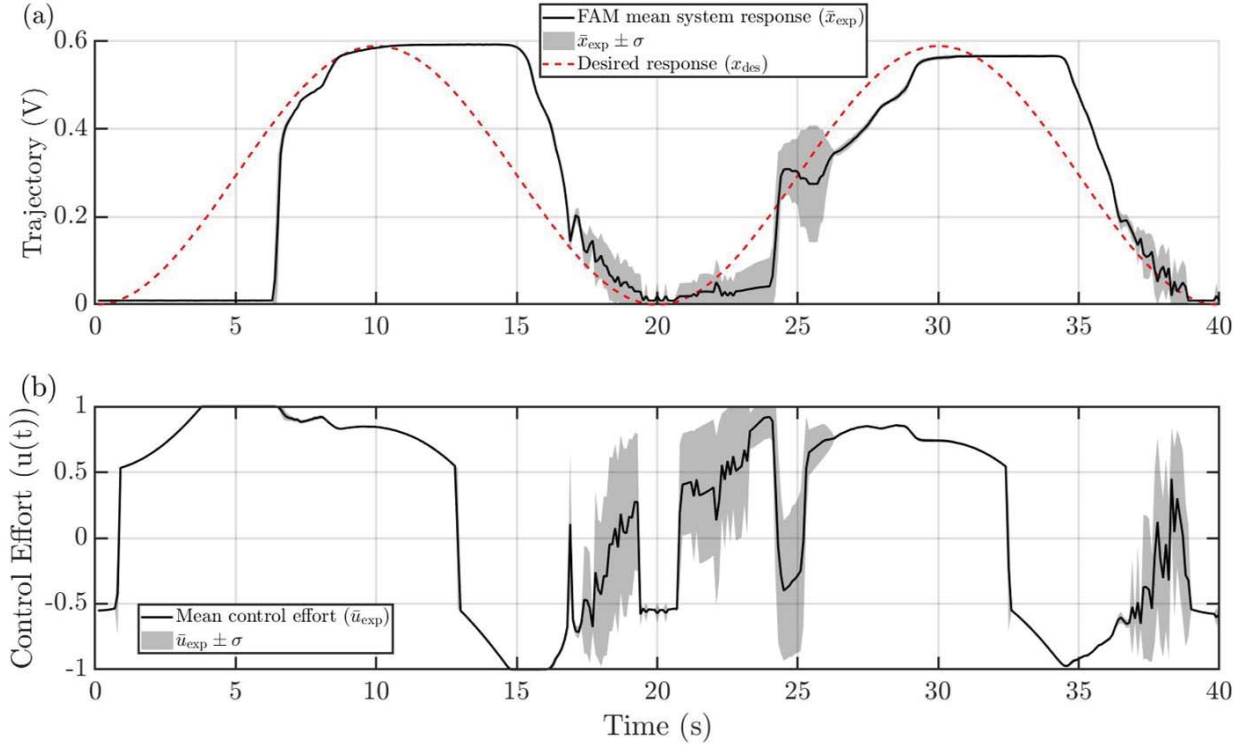
Figure 34: Test finger under PI control (a) Sensor Position (b) Control Effort. There is delay within the system, but the joint is able to flex and extend.

5.3 Wearable Exoskeleton Design

The components used to actuate the finger model are transferable to a wearable exoskeleton. The distal and proximal plug, the medial hydraulic connection, and the restoring force sheath can be fitted to a plastic wrist splint, cut to cover only the palm, and a glove. The wearable exoskeleton would therefore have the same functionality as that achieved by the exoskeleton fitted to the model finger. Once prototypes of the wearable exoskeleton are completed, preliminary testing in healthy human subjects can begin with the approval of the Human Research Protection Program (HRPP).

6 Conclusions

To create a device actuated by FAMs and capable of guiding the hand through the positions of tendon glide, a novel model was developed and linear and adaptive controls were applied to FAMs in both simulation and experimentation. The FAMs discussed in this paper were not well described by existing models. Therefore, the fixed-end cylindrical model was developed, which accurately represents the contraction of small FAMs well suited for rehabilitation devices. The fixed-end cylindrical model assumes the center portion of the FAM contracts according to the pantographic opening principle, while the ends remain a fixed length but expand and consume fluid. The model enabled the accurate simulation of FAM dynamics, which aided in the development and tuning of linear and adaptive controllers.

MRAC and PI controllers were simulated, tuned, and tested in experimentation to govern the contraction of the FAM. Both controllers enabled the system to track three kinds of input signals: a step, ramp, and sinusoid. The MRAC demonstrated consistently less tracking error than the PI controller, but also exhibited oscillatory behavior. The PI controller, despite lag, mimicked the shape of the reference system. In order to ensure that a patients hand is moved smoothly and with minimal oscillations, the PI controller was chosen for implementation in a rehabilitation device.

A rehabilitation exoskeleton was capable of achieving all five positions of tendon glide for a test finger. The exoskeleton applied to the test finger is transferable to a wearable device. Implementation of a PI controller to track a sinusoidal reference system enabled the joint to flex and extend in a controllable manner. The device did not accurately track the reference system, indicating an adaptive, rather than a linear, controller may be necessary. The MRAC exhibited oscillatory behavior. Therefore, a control scheme that incorporates linear and adaptive algorithms could achieve the error tracking of the MRAC with the smooth response of the PI controller. One potential option is the Augmented Adaptive PI Controller [Jaramillo Cienfuegos et al., 2017].

7 Project Impact and Contributions

This project originally proposed to meet a series of goals in pursuit of a wearable exoskeleton capable of achieving the positions of tendon glide. Those goals and the corresponding deliverables are shown below, along with the results of the project.

Goal 1: Build, model, and control McKibben muscle for exoskeleton application
> **Deliverable:** McKibben muscles capable of contracting 1 cm under minimal pressure.
> **Result:** McKibben muscles capable of of achieving greater than 0.2 strain.

> **Deliverable:** A mathematical model representing the dynamics of the McKibben muscle based on measured input and output information across the frequency spectrum.
> **Result:** A mathematical model, called the fixed-end cylindrical model, relating the volume change of a FAM to the position of the FAM, regardless of load.

> **Deliverable:** Linear Proportional Integral and nonlinear Model Reference Adaptive algorithms for tracking McKibben muscle contraction with minimal error.
> **Result:** Linear Proportional Integral and nonlinear Model Reference Adaptive algorithms capable of tracking McKibben muscle contraction with minimal tracking error.

> **Deliverable:** Submit findings and present results of the open-loop and closed-loop simulations and experiments at a conference.

Result: Publication accepted with revisions to the International Journal of Robotics Research, Special Issue on Soft Robotics Modeling and Control: Bringing Together Articulated Soft Robotics and Soft-Bodied Robots.

Goal 2: Adapt and model a plunger-syringe system for actuating McKibben muscles
Deliverable: A hydraulic system capable of supplying 300 KPa of pressure and 2 mL of fluid, while minimizing cross-sectional area.
Result: A hydraulic system capable of supplying well over 300 KPa of pressure and 25 mL of fluid.

Deliverable: A mathematical model representing the dynamics of the hydraulic system based on measured input and output data.
Result: A pump model based on first principles.

Goal 3: Design, build, and control an exoskeleton system for one finger
Deliverable: A wearable exoskeleton driven for one finger for open-loop hand motion.
Result: An exoskeleton fitted to a test finger for human-in-the-loop achievement of the positions of tendon glide.

Deliverable: A wearable exoskeleton to be guided by a linear and a nonlinear controller for best tracking performance. The system is capable of tracking the motions based on the tendon glide exercise routine.
Result: An exoskeleton fitted to a test finger able to flex and extend a joint when governed by linear control.

Deliverable: A manuscript for submission to a journal, such as *IEEE Journal of Robotics and Automation*, *Journal of Mechanisms and Robotics*, or the *Journal of Rehabilitation and Assistive Technologies Engineering*, etc.
Result: A manuscript to disseminate the full results of the project in progress. A publication accepted with revisions to the International Journal of Robotics Research, Special Issue on Soft Robotics Modeling and Control: Bringing Together Articulated Soft Robotics and Soft-Bodied Robots.

8   Dissemination of Current Research Work

Below is a bibliography of articles, posters, and presentations done in conjunction with this work.

[1] **Anderson Camp**, Edward Chapman, Paola Jaramillo Cienfuegos. (2019, Apr.). "Modeling and analysis of hydraulic piston actuation of McKibben fluidic artificial muscles for hand rehabilitation." *International Journal of Robotics Research.* Accepted with revisions.

[2] **Anderson Camp**, Edward M. Chapman, and Paola Jaramillo Cienfuegos. Rehabilitation "Exoskeleton for the Hand," presentation given at Biomedical Engineering Seminar, USNA, Annapolis, MD, 2019.

[3] **Anderson Camp**, Edward M. Chapman, and Paola Jaramillo Cienfuegos. "Coupled Piston-McKibben Model for and Control of McKibben Muscles in Rehabilitation Devices," poster presented at USNA Poster Session, Annapolis, MD, 2018.

[4] **Anderson Camp**, Edward M. Chapman, and Paola Jaramillo Cienfuegos. "Development of Input/Output based Model for the Implementation of McKibben Muscles in Rehabilitation Devices," poster presented at BMES Annual meeting, Atlanta, GA, 2018.

[5] **Anderson Camp** and Paola Jaramillo Cienfuegos. "A lightweight prosthetic finger actuated by nitinol springs," poster presented at MAMNA, Laurel, MD, 2017.

[6] **Anderson Camp** and Paola Jaramillo Cienfuegos. "Development of an At-Home Assistive Rehabilitation Hand Exoskeleton Guided by Feedback," poster presented at USNA Poster Session, Annapolis, MD, 2017.

References

Priyanshu Agarwal, Jonas Fox, Youngmok Yun, Marcia K. O'Malley, and Ashish D. Deshpande. An index finger exoskeleton with series elastic actuation for rehabilitation: Design, control and performance characterization. *International Journal of Robotics Research*, 34(14):1747–1772, 2015. ISSN 17413176. doi: 10.1177/0278364915598388.

Ho Pham Huy Anh and Kyoung Kwan Ahn. Hybrid control of a pneumatic artificial muscle (PAM) robot arm using an inverse NARX fuzzy model. *Engineering Applications of Artificial Intelligence*, 24(4):697–716, 2011. ISSN 09521976. doi: 10.1016/j.engappai.2010.11.007.

Alan T. Asbeck, Stefano M.M. De Rossi, Kenneth G. Holt, and Conor J. Walsh. A biologically inspired soft exosuit for walking assistance. *International Journal of Robotics Research*, 34(6): 744–762, 2015. ISSN 17413176. doi: 10.1177/0278364914562476.

Alberto Borboni, Jorge H. Villafañe, Chiara Mullè, Kristin Valdes, Rodolfo Faglia, Giovanni Taveggia, and Stefano Negrini. Robot-Assisted Rehabilitation of Hand Paralysis After Stroke Reduces Wrist Edema and Pain: A Prospective Clinical Trial. *Journal of Manipulative and Physiological Therapeutics*, 40(1):21–30, 2017. ISSN 15326586. doi: 10.1016/j.jmpt.2016.10.003.

K. Braikia, B. Tondu, M. Chettouh, P. Acco, and M. Hamerlain. Improved Control Strategy of 2-Sliding Controls Applied to a Flexible Robot Arm. *Advanced Robotics*, 25(11-12):1515–1538, 2011. ISSN 0169-1864. doi: 10.1163/016918611x579510.

Dawei Cai. A Sliding Mode Controller for Manipulator Driven by Artificial Muscle Actuator. In *Proceedings of the 2000 IEEE international Conference on Control Applications*, pages 668–673, 2000. ISBN 0780365623.

S. W. Chan, John H. Lilly, Daniel W. Repperger, and James E. Berlin. Fuzzy PD+I learning control for a pneumatic muscle. In *The IEEE International Conference on Fuzzy Systems*, pages 278–283, 2004. ISBN 0780378105. doi: 10.1109/fuzz.2003.1209375.

Edward M. Chapman and Matthew Bryant. Bioinspired passive variable recruitment of fluidic artificial muscles. *Journal of Intelligent Material Systems and Structures*, 29(15):3067–3081, 2018. ISSN 15308138. doi: 10.1177/1045389X18783070.

Edward M. Chapman, Tyler E. Jenkins, and Matthew Bryant. Modeling and analysis of a meso-hydraulic climbing robot with artificial muscle actuation. *Bioinspiration and Biomimetics*, 12 (6), 2017. ISSN 17483190. doi: 10.1088/1748-3190/aa7eb0.

Ching-Ping Chou and Blake Hannaford. Measurement and Modeling of McKibben Pneumatic Artifical Muscles. *IEEE Transcations on Robotics and Automation*, 22(1):90–102, 1996. ISSN 09310509. doi: 10.1093/ndt/gfm531.

M. De Volder, A.J.M. Moers, and D. Reynaerts. Fabrication and control of miniature McKibben actuators. *Sensors and Actuators, A: Physical*, 166(1):111–116, 2011. ISSN 09244247. doi: 10.1016/j.sna.2011.01.002.

J a Dent. Continuous passive motion in hand rehabilitation. *Prosthetics and orthotics international*, 17:130–135, 1993. ISSN 03093646. doi: 10.3109/03093649309164369.

Richard C. Dorf and Robert H. Bishop. *Modern Control Systems*. Prentice-Hall, Upper Saddle River, NJ, 5th editio edition, 2010.

Dwain R. Faso and Mel Stills. Passive Mobilization: An Orthotist's Overview. *Clinical Prosthetics and Orthotics*, 9(2):7–19, 1975.

Valery L. Feigin, Carlene MM Lawes, Derrick A. Bennett, Suzanne L. Barker-Collo, and Varsha Parag. Worldwide stroke incidence and early case fatality reported in 56 population-based studies: a systematic review. *The Lancet Neurology*, 8(4):355–369, 2009. ISSN 14744422. doi: 10.1016/S1474-4422(09)70025-0.

Michele Focchi, Emanuele Guglielmino, Claudio Semini, Alberto Parmiggiani, Nikos Tsagarakis, Bram Vanderborght, and Darwin G. Caldwell. Water/air performance analysis of a fluidic muscle. *IEEE/RSJ 2010 International Conference on Intelligent Robots and Systems, IROS 2010 - Conference Proceedings*, pages 2194–2199, 2010. ISSN 2153-0858. doi: 10.1109/IROS.2010.5650432.

Abhishek Gupta, Marcia K. O'Malley, Volkan Patoglu, and Charles Burgar. Design, control and performance of RiceWrist: A force feedback wrist exoskeleton for rehabilitation and training. *International Journal of Robotics Research*, 27(2):233–251, 2008. ISSN 01763679. doi: 10.1055/s-0029-1224138.

Henk T. Hendricks, Jacques Van Limbeek, Alexander C. Geurts, and Machiel J. Zwarts. Motor recovery after stroke: A systematic review of the literature. *Archives of Physical Medicine and Rehabilitation*, 83(11):1629–1637, 2002. ISSN 00039993. doi: 10.1053/apmr.2002.35473.

Ted Hesselroth, Kakali Sarkar, Patrick Van Der Smagt, and Klaus Schulten. Neural Network Control of a Pneumatic Robot Arm. *IEEE Transactions on Systems Man and Cybernetics*, 1994. doi: 10.1109/21.259683.

Petros Ioannou and Jing Sun. *Robust Adaptive Control*. Prentice-Hall, NJ, 1996.

Paola Jaramillo Cienfuegos, Adam Shoemaker, Robert W Grange, Nicole Abaid, and Alexander Leonessa. Classical and adaptive control of ex vivo skeletal muscle contractions using functional electrical stimulation (FES). *PLoS ONE*, 12(3):1–29, 2017. ISSN 19326203.

Ville T. Jouppila, S. Andrew Gadsden, Gary M. Bone, Asko U. Ellman, and Saeid R. Habibi. Sliding mode control of a pneumatic muscle actuator system with a PWM strategy. *International Journal of Fluid Power*, 15(1):19–31, 2014. ISSN 1439-9776. doi: 10.1080/14399776.2014.893707.

Bongsu Kim and Ashish D. Deshpande. An upper-body rehabilitation exoskeleton Harmony with an anatomical shoulder mechanism: Design, modeling, control, and performance evaluation. *International Journal of Robotics Research*, 36(4):414–435, 2017. ISSN 17413176. doi: 10.1177/0278364917706743.

Curt S. Kothera, Mamta Jangid, Jayant Sirohi, and Norman M. Wereley. Experimental Characterization and Static Modeling of McKibben Actuators. *Journal of Mechanical Design*, 131(9): 091010, 2009. ISSN 10500472. doi: 10.1115/1.3158982.

Nancy G. Kutner, Rebecca Zhang, Andrew J. Butler, Steven L. Wolf, and Jay L. Alberts. Quality-of-Life Change Associated With Robotic-Assisted Therapy to Improve Hand Motor Function in Patients With Subacute Stroke: A Randomized Clinical Trial. *Physical Therapy*, 90(4):493–504, 2010. ISSN 0031-9023. doi: 10.2522/ptj.20090160.

Cecilia Laschi and Matteo Cianchetti. Soft Robotics: New Perspectives for Robot Bodyware and Control. *Frontiers in Bioengineering and Biotechnology*, 2(January):1–5, 2014. ISSN 2296-4185. doi: 10.3389/fbioe.2014.00003.

Alistair C. McConnell, Marta Vallejo, Renan Cipriano Moioli, Fabricio L. Brasil, Nicola Secciani, Markus P. Nemitz, Cecile P. Riquart, David W. Corne, Patricia A. Vargas, and Adam A. Stokes. SOPHIA: Soft Orthotic Physiotherapy Hand Interactive Aid. *Frontiers in Mechanical Engineering*, 2017. ISSN 2297-3079. doi: 10.3389/fmech.2017.00003.

Michael A. Meller, Matthew Bryant, and Ephrahim Garcia. Reconsidering the McKibben muscle: Energetics, operating fluid, and bladder material. *Journal of Intelligent Material Systems and Structures*, 25(18):2276–2293, 2014. ISSN 15308138. doi: 10.1177/1045389X14549872.

Kumpati S. Narendra and Anuradha M. Annasway. *Stable Adaptive Systems*. Prentice-Hall, Englewood Cliffs, NJ, 1989.

A. S. Nouri, CH. Gauvert, B. Tondu, and P. Lopez. Generalized variable structure model reference adaptive control of one-link artificial muscle manipulator in two operating modes. In *Proceedings of IEEE International Conference on Systems, Man and Cybernetics*, pages 1944–1950, 2002. ISBN 0780321294. doi: 10.1109/icsmc.1994.400136.

Katsuhiko Ogata. *Modern Control Engineering*. Prentice-Hall, Upper Saddle River, NJ, 5th editio edition, 2009.

Rolf Pfeifer, Max Lungarella, and Fumiya Iida. The challenges ahead for bio-inspired 'soft' robotics. *Communications of the ACM*, 55(11):76, 2012. ISSN 00010782. doi: 10.1145/2366316.2366335.

Panagiotis Polygerinos, Zheng Wang, Kevin C. Galloway, Robert J. Wood, and Conor J. Walsh. Soft robotic glove for combined assistance and at-home rehabilitation. *Robotics and Autonomous Systems*, 73:135–143, 2015. ISSN 09218890. doi: 10.1016/j.robot.2014.08.014.

Angelica Ruszkowski, Omid Mohareri, Sam Lichtenstein, Richard Cook, and Septimiu Salcudean. On the feasibility of heart motion compensation on the daVinci® surgical robot for coronary artery bypass surgery: Implementation and user studies. *Proceedings - IEEE International Conference on Robotics and Automation*, 2015-June(June):4432–4439, 2015. ISSN 10504729. doi: 10.1109/ICRA.2015.7139812.

Dongseok Ryu, Kyung Won Moon, Hyungdo Nam, Yongkwun Lee, Changmook Chun, Sungchul Kang, and Jea Bok Song. Micro hydraulic system using slim artificial muscles for a wearable haptic glove. In *2008 IEEE/RSJ International Conference on Intelligent Robots and Systems, IROS*, 2008. ISBN 9781424420582. doi: 10.1109/IROS.2008.4651159.

Xiangrong Shen. Control Engineering Practice Nonlinear model-based control of pneumatic artificial muscle servo systems. *Control Engineering Practice*, 18(3):311–317, 2010. ISSN 0967-0661. doi: 10.1016/j.conengprac.2009.11.010.

Craig D. Takahashi, Lucy Der-Yeghiaian, Vu Le, Rehan R. Motiwala, and Steven C. Cramer. Robot-based hand motor therapy after stroke. *Brain*, 131(2):425–437, 2008. ISSN 14602156. doi: 10.1093/brain/awm311.

TU Diep Cong Thanh and Kyoung Kwan Ahn. Nonlinear PID control to improve the control performance of 2 axes pneumatic artificial muscle manipulator using neural network. *Mechatronics*, 16(9):577–587, 2006. ISSN 09574158. doi: 10.1016/j.mechatronics.2006.03.011.

UVA HAND CENTER – THERAPY. Open Carpal Tunnel Release Post-Op Guidelines.

Kelly O Thielbar, Thomas J Lord, Heidi C Fischer, Emily C Lazzaro, Kristin C Barth, Mary E Stoykov, Kristen M Triandafilou, and Derek G Kamper. Training finger individuation with a mechatronic-virtual reality system leads to improved fine motor control post-stroke. *Journal of NeuroEngineering and Rehabilitation*, 11(1):171, 2014. doi: 10.1186/1743-0003-11-171.

Rashi Tiwari, Michael A. Meller, Karl B. Wajcs, Caris Moses, Ismael Reveles, and Ephrahim Garcia. Hydraulic artificial muscles. *Journal of Intelligent Material Systems and Structures*, 23 (3):301–312, 2012. ISSN 1045389X. doi: 10.1177/1045389X12438627.

Bertrand Tondu. Modelling of the McKibben artifical muscle: A review. *Journal of Intelligent Material Systems and Structures*, 23(3):225–253, 2012. ISSN 1045389X. doi: 10.1177/1045389X11435435.

Bertrand Tondu. Robust and Accurate Closed-Loop Control of McKibben Artificial Muscle Contraction with a Linear Single Integral Action. *Actuators*, pages 142–161, 2014. doi: 10.3390/act3020142.

Bertrand Tondu and Pierre Lopez. Modeling and Control of McKibben Artificial Muscle Robot Actuators. *IEEE Control Systems*, 20(2):15–38, 2000. ISSN 1066033X. doi: 10.1109/37.833638.

B. T. Volpe, H. I. Krebs, N. Hogan, L. Edelsteinn, C. M. Diels, and M. L. Aisen. Robot training enhanced motor outcome in patients with stroke maintained over 3 years. *Neurology*, 53(8): 1874–6, nov 1999. ISSN 0028-3878. doi: 10.1212/W.

Marwan A Wehbe. Tendon Gliding. *The American Journal of Occupational Therapy*, 41(3):164–167, 1987.

Steven L. Wolf, Carolee J. Winstein, J. Philip Miller, and David Morris. Effect of Constraint-Induced Movement. *JAMA*, 296(17):2095–2104, 2011.

David Wooden, Matthew Malchano, Kevin Blankespoor, Andrew Howard, Alfred A Rizzi, and Marc Raibert. Autonomous Navigation for BigDog. pages 4736–4741, 2010. ISSN 10504729. doi: 10.1109/ROBOT.2010.5509226.

Xiaocong Zhu, Guoliang Tao, Bin Yao, and Jian Cao. Adaptive robust posture control of a parallel manipulator driven by pneumatic muscles. *Automatica*, 44(9):2248–2257, 2008. ISSN 00051098. doi: 10.1016/j.automatica.2008.01.015.

9 Supplemental Material

Figure S1 shows the experimental data for all the loads tested with the Tondu cylindrico-conical strain predictions. For the FAMs tested in this paper, the model does not accurately predict the strain.
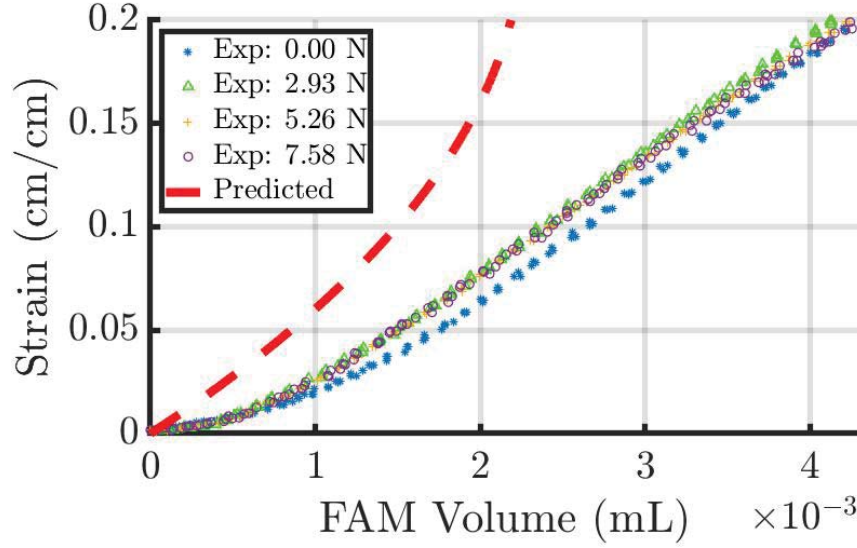
Figure S1: Discrepancy between adapted Tondu cylindrico-conical model and experimental data. The cylindrico-conical model overpredicts the strain of the FAM for a given volume.

Figure S2 shows the experimental data for all the loads tested with the fixed-end strain predictions. The fixed-end model successfully predicts the strain for all loads.
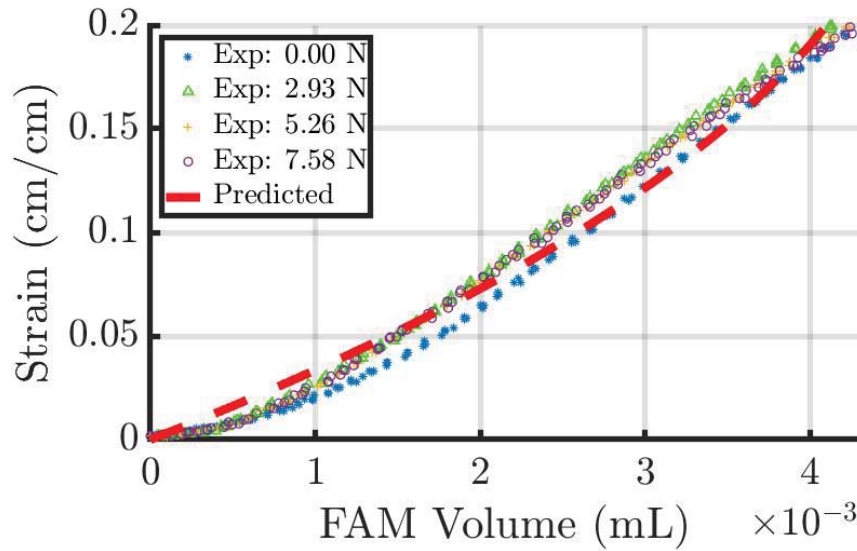

Figure S2: Validation of fixed-end cylindrical model. The model generally matches the experimental data.

A Appendix

A.1 Code used for MRAC and PI control in the linear test bed

```
1    #include "mbed.h"
2    #include "SDFileSystem.h"
3
4    SDFileSystem sd(p5, p6, p7, p8, "sd"); // the pinout on the mbed Cool Components
     workshop board
5    Ticker c;//control
6    Ticker d;//was for data
7    Serial pc(USBTX,USBRX);
8    DigitalOut en(p18);//Motor Control
9    DigitalOut dr(p19);//Motor control
10   PwmOut st(p21);//Motor
11   AnalogIn distance(p15);//FAM pos
12   AnalogIn pressure(p16);//use for pressure sensor
13   AnalogIn touch(p17);//used for syringe pump pressure detection
14   DigitalOut ct(p11);//for oscope flag
15   DigitalOut dt(p12);//for oscope flag
16
17   float t=0;  //time
18   float desired; //for controller
19   float dist0;  //for strain calc
20   float strain;
21   float er = 0;  //for running error
22   float er0;
23   float PWM;     //for running error
24   float period = .01; //control update period
25   float eri = 0;  //for integral of error
26   float kp = 2.35; //proportional gain
27   float ki = .28;    // integral gain
28   int signal;    //Control Effort
29   float dist;     //Pot position
30   int e;          //for data export
31   FILE *fp;       //for SPI export
32   char filename[30];  //to call SPI file
33   float timei;    //for integral
34   float r = 0;    //mrac reference
35   float rd;       //reference derivative
36   float rd0 = 0;  //for running integral
37   float theta_xd0 = 0;    //for running integral
38   float theta_rd0 = 0;    //for running integral
39   float theta_xd;     //gain derivative
40   float theta_rd;     //gain derivative
41   float tx = 0;   //gain
42   float tr = 0;   //gain
43   float ar = -.5;     //reference model
44   float br = .5;      //reference model
45   float gr = 1000;     //tuning parameter
46   float gx = 900;      //tuning parameter
47   int loopcount = 0;  //for data export
48   int dout;       //for data export
49   int txout;      //for data export
50   int trout;      //for data export
51
52   void PIStep()   //PI control for step
53   {
54       ct = 1;     //Triggers for OScope
55       ct = 0;
56       ct = 1;
57       strain = (distance*3.3 - dist0)/2.12598425; //strain based on 54 mm
58       er0 = desired - strain; //error
59       eri = eri + ((er0+er)*period)/2.0; //integral of error
60       er = er0;   //stores last value
61       PWM = (eri * ki) + (er0 * kp); //PI control law
62       if(PWM>0) { //assigns direction
63           dr = 1;
64       } else {
65           dr = 0;
66       }
67       st = abs(PWM)+.53; //addition to beat friction
68       ct = 0;     //for data export
```

```
69        loopcount = loopcount + 1;
70        if( loopcount == 10) {
71            if(PWM>0) {
72                signal = (PWM + .53)*1000;
73            } else {
74                signal = (PWM - .53)*1000;
75            }
76            e = strain*1000.0;
77            dout = desired*1000.0;
78            fprintf(fp, "%d,%d,%d\n\r",e,signal,dout);
79            loopcount = 0;
80        }
81    }
82
83    void PIRamp()
84    {
85        strain = (distance*3.3 - dist0)/2.12598425; //strain based on 53 mm
86        desired = t*.02;      //ramp
87        if(desired>.2) {      //max value of ramp
88            desired = .2;
89        }
90        er0 = desired - strain; //error
91        eri = eri + ((er0+er)*period)/2.0;   //integral
92        er = er0;    //stores
93        PWM = (eri * ki) + (er0 * kp); //control law
94        if(PWM>0) { //assigns direction
95            dr = 1;
96        } else {
97            dr = 0;
98        }
99        st = abs(PWM)+.53; //boost for friction
100       t = t + period; //assigns time
101       loopcount = loopcount + 1; //for data export
102       if( loopcount == 10) {
103           if(PWM>0) {
104               signal = (PWM + .53)*1000;
105           } else {
106               signal = (PWM - .53)*1000;
107           }
108           e = strain*1000.0;
109           dout = desired*1000.0;
110           fprintf(fp, "%d,%d,%d\n\r",e,signal,dout);
111           loopcount = 0;
112       }
113   }
114
115   void PISin()
116   {
117       strain = (distance*3.3 - dist0)/2.12598425; //strain based on 54 mm
118       desired = -.1*cos(.314159265*t)+.1; //sin signal
119       er0 = desired - strain; //error
120       eri = eri + ((er0+er)*period)/2.0; //integral
121       er = er0; //stores value
122       PWM = (eri * ki) + (er0 * kp); //control law
123       if(PWM>0) { //assigns direction
124           dr = 1;
125       } else {
126           dr = 0;
127       }
128       st = abs(PWM)+.53; //boost for friction
129       t = t + period; //time
130       loopcount = loopcount + 1; //for data export
131       if( loopcount == 10) {
132           if(PWM>0) {
133               signal = (PWM + .53)*1000;
134           } else {
135               signal = (PWM - .53)*1000;
136           }
137           e = strain*1000.0;
```

```
138            dout = desired*1000.0;
139            fprintf(fp, "%d,%d,%d\n\r",e,signal,dout);
140            loopcount = 0;
141        }
142    }
143
144    void MStep()
145    {
146        ct = 1; //flag for oscope
147        ct = 0;
148        ct = 1;
149        strain = (distance*3.3 - dist0)/2.12598425; //strain defined based on 54 mm
150        rd = ar*r + br*desired; //d ofreference signal
151        r = r + ((rd+rd0)*period)/2.0; //integral
152        rd0 = rd;//stores value
153        er = r - strain;//error
154        theta_xd = -gx*er*strain; //derivative of gains
155        theta_rd = -gr*er*r;        //
156        tr = tr + ((theta_rd+theta_rd0)*period)/2.0; //integrate gains
157        tx = tx + ((theta_xd+theta_xd0)*period)/2.0;
158        theta_xd0 = theta_xd; //stores values
159        theta_rd0 = theta_rd;
160        PWM = tx*strain + tr*desired; //control law
161        PWM = -1.0*PWM; //flips sign
162        if(PWM>0) {//assign directions
163            dr = 1;
164        } else {
165            dr = 0;
166        }
167        st = abs(PWM)+.53;//bosts for fritction
168        ct = 0; //flag for oscope
169        loopcount = loopcount + 1;//for data export
170        if( loopcount == 10) {
171            if(PWM>0) {
172                signal = (PWM + .53)*1000;
173            } else {
174                signal = (PWM - .53)*1000;
175            }
176            e = strain*1000.0;
177            dout = r*1000.0;
178            txout = tx*1000.0;
179            trout = tr*1000.0;
180            fprintf(fp, "%d,%d,%d,%d,%d\n\r",e,signal,dout,txout,trout);
181            loopcount = 0;
182        }
183    }
184
185    void MRamp()
186    {
187        desired = t*.02;
188        strain = (distance*3.3 - dist0)/2.12598425; //strain defined based on 54 mm
189        rd = ar*r + br*desired; //d ofreference signal
190        r = r + ((rd+rd0)*period)/2.0; //integral
191        rd0 = rd;//stores value
192        er = r - strain;//error
193        theta_xd = -gx*er*strain; //derivative of gains
194        theta_rd = -gr*er*r;        //
195        tr = tr + ((theta_rd+theta_rd0)*period)/2.0; //integrate gains
196        tx = tx + ((theta_xd+theta_xd0)*period)/2.0;
197        theta_xd0 = theta_xd; //stores values
198        theta_rd0 = theta_rd;
199        PWM = tx*strain + tr*desired; //control law
200        PWM = -1.0*PWM; //flips sign
201        if(PWM>0) {//assign directions
202            dr = 1;
203        } else {
204            dr = 0;
205        }
206        st = abs(PWM)+.53;//bosts for fritction
```

```
207        t = t + period; //time
208        loopcount = loopcount + 1;//for data export
209        if( loopcount == 10) {
210            if(PWM>0) {
211                signal = (PWM + .53)*1000;
212            } else {
213                signal = (PWM - .53)*1000;
214            }
215            e = strain*1000.0;
216            dout = r*1000.0;
217            txout = tx*1000.0;
218            trout = tr*1000.0;
219            fprintf(fp, "%d,%d,%d,%d,%d\n\r",e,signal,dout,txout,trout);
220            loopcount = 0;
221        }
222    }
223
224    void MSin()
225    {
226        desired = -.1*cos(.314159265*t)+.1;
227        strain = (distance*3.3 - dist0)/2.12598425; //strain defined based on 54 mm
228        rd = ar*r + br*desired; //d ofreference signal
229        r = r + ((rd+rd0)*period)/2.0; //integral
230        rd0 = rd;//stores value
231        er = r - strain;//error
232        theta_xd = -gx*er*strain; //derivative of gains
233        theta_rd = -gr*er*r;        //
234        tr = tr + ((theta_rd+theta_rd0)*period)/2.0; //integrate gains
235        tx = tx + ((theta_xd+theta_xd0)*period)/2.0;
236        theta_xd0 = theta_xd; //stores values
237        theta_rd0 = theta_rd;
238        PWM = tx*strain + tr*desired; //control law
239        PWM = -1.0*PWM; //flips sign
240        if(PWM>0) {//assign directions
241            dr = 1;
242        } else {
243            dr = 0;
244        }
245        st = abs(PWM)+.53;//bosts for fritction
246        t = t + period; //time
247        loopcount = loopcount + 1; //for data export
248        if( loopcount == 10) {
249            if(PWM>0) {
250                signal = (PWM + .53)*1000;
251            } else {
252                signal = (PWM - .53)*1000;
253            }
254            e = strain*1000.0;
255            dout = r*1000.0;
256            txout = tx*1000.0;
257            trout = tr*1000.0;
258            fprintf(fp, "%d,%d,%d,%d,%d\n\r",e,signal,dout,txout,trout);
259            loopcount = 0;
260        }
261    }
262
263    int main()
264    {
265        NVIC_SetPriority(TIMER3_IRQn, 1);//bumps up ticker priority
266        st.period(.00005); //PWM period
267        wait(.1); //give time
268        en = 1; // turn motor "on"
269        getchar(); //get key
270        dr = 1; //forward
271        st = 1; //100%
272        wait(.25); //for a burst
273        dr = 0; //go in reverse
274        while(touch < .22) { //until the system is unpressed
275            wait(.01);
```

```
276            st = .75;
277        }
278        dr = 1; //go forward
279        wait(.01); //stops backward motion
280        st = 0; //stop
281        desired = .2; //0.2 strain
282        wait(.3); //let settle
283        printf("Ready");
284        getchar(); //get key
285        for(int i = 1; i < 1; i++) { //do PI control for a step x number of times
286            sprintf(filename, "/sd/PIStep%d.txt", i);
287            fp = fopen(filename, "w");  // open for writing
288            dist0 = distance * 3.3; //starting point
289            eri = 0; //resets integral values
290            er = 0;
291            t = 0;
292            loopcount = 0; //resets data export counter
293            c.attach(&PIStep,period); //do control
294            wait(20.5); //for 20.5s
295            c.detach(); //stop
296            st = 0;
297            dr = 0;
298            while(touch < .22) { //tke pressure off
299                wait(.01);
300                st = .75;
301            }
302            dr = 1;
303            wait(.01);
304            st = 0;
305            wait(2);
306            fclose(fp); //close file
307        }
308        for(int i = 1; i < 1; i++) { // do PI control for ramp
309            sprintf(filename, "/sd/PIRamp%d.txt", i);
310            fp = fopen(filename, "w");  // open for writing
311            dist0 = distance * 3.3; //start point
312            eri = 0; //reset running values
313            er = 0;
314            t = 0;
315            loopcount = 0;
316            c.attach(&PIRamp,period); //do control
317            wait(20.5); //for 20.5 s
318            c.detach(); //stop
319            st = 0;
320            dr = 0;
321            while(touch < .22) {//take pressure off
322                wait(.01);
323                st = .75;
324            }
325            dr = 1;
326            wait(.01);
327            st = 0;
328            wait(2);
329            fclose(fp);//close file
330        }
331        for(int i = 1; i < 1; i++) { //do PI control for sin
332            sprintf(filename, "/sd/PISin%d.txt", i);
333            fp = fopen(filename, "w");  // open for writing
334            dist0 = distance * 3.3; //starting point
335            eri = 0; //reset running values
336            er = 0;
337            t = 0;
338            loopcount = 0;
339            c.attach(&PISin,period); //do control
340            wait(40.5); // for 40.5s
341            c.detach(); //stop
342            st = 0;
343            dr = 0;
344            while(touch < .22) { //take pressure off
```

```
345             wait(.01);
346             st = .75;
347         }
348         dr = 1;
349         wait(.01);
350         st = 0;
351         wait(2);
352         fclose(fp); //close file
353     }
354     for(int i = 1; i < 1; i++) { //do MRAC for step
355         sprintf(filename, "/sd/MStep%d.txt", i);
356         fp = fopen(filename, "w");  // open for writing
357         dist0 = distance * 3.3;/ starting point
358         r = 0; //reset all values
359         t = 0;
360         rd = 0;
361         rd0 = 0;
362         theta_xd0 = 0;
363         theta_rd0 = 0;
364         theta_xd = 0;
365         theta_rd = 0;
366         tx = 7; //inital conditions
367         tr = -7;
368         loopcount = 0;
369         desired = .2; //.2 strain
370         c.attach(&MStep,period); // do control
371         wait(20.5);//for 20.5 s
372         c.detach();//stop
373         st = 0;
374         dr = 0;
375         while(touch < .22) {//take pressure off
376             wait(.01);
377             st = .75;
378         }
379         dr = 1;
380         wait(.01);
381         st = 0;
382         wait(2);
383         fclose(fp);//close file
384     }
385     for(int i = 1; i < 1; i++) {// MRAC ramp
386         sprintf(filename, "/sd/MRamp%d.txt", i);
387         fp = fopen(filename, "w");  // open for writing
388         dist0 = distance * 3.3; //starting point
389         r = 0; //reset all values
390         t = 0;
391         rd = 0;
392         rd0 = 0;
393         theta_xd0 = 0;
394         theta_rd0 = 0;
395         theta_xd = 0;
396         theta_rd = 0;
397         tx = 7; //initial conditions
398         tr = -7;
399         loopcount = 0;
400         c.attach(&MRamp,period);//do control
401         wait(20.5);//for 20.5s
402         c.detach();// stop
403         st = 0;
404         dr = 0;
405         while(touch < .22) {//take pressure off
406             wait(.01);
407             st = .75;
408         }
409         dr = 1;
410         wait(.01);
411         st = 0;
412         wait(2);
413         fclose(fp);//close file
```

```
414          }
415      for(int i = 1; i < 5; i++) {//do MRAC for sin
416          sprintf(filename, "/sd/MSinLong%d.txt", i);
417          fp = fopen(filename, "w");  // open for writing
418          dist0 = distance * 3.3;//starting point
419          r = 0;       // reset all values
420          t = 0;
421          rd = 0;
422          rd0 = 0;
423          theta_xd0 = 0;
424          theta_rd0 = 0;
425          theta_xd = 0;
426          theta_rd = 0;
427          tx = 7;//initial conditions
428          tr = -7;
429          loopcount = 0;
430          c.attach(&MSin,period);//do control
431          wait(80.5);//for 80.5 seconds
432          c.detach();//stop
433          st = 0;
434          dr = 0;
435          while(touch < .22) {//take pressure off
436              wait(.01);
437              st = .75;
438          }
439          dr = 1;
440          wait(.01);
441          st = 0;
442          wait(2);
443          fclose(fp);//close file
444      }
445  }
446
```

A.2 Code used for PI control of the test finger

```
1    #include "mbed.h"
2    #include "SDFileSystem.h"
3
4    SDFileSystem sd(p5, p6, p7, p8, "sd"); // the pinout on the mbed Cool Components
     workshop board
5    Ticker c; //for control
6    Serial pc(USBTX,USBRX);
7    DigitalOut en(p18); //for motor control
8    DigitalOut dr(p19); //for motor control
9    PwmOut st(p21); //Motor PWM
10   AnalogIn pos1(p15); //finger position
11   AnalogIn touch(p17); //load on plunger
12
13   float t=0; //time
14   float desired; //desired position
15   float er = 0; //error
16   float er0; //for integral
17   float PWM; //motor signal
18   float period = .01; //control period
19   float eri = 0; //for integral error
20   float kp = 2.35; //Porp gain
21   float ki = .28; //Int gain
22   int signal; //for data export
23   int e; //for data export
24   FILE *fp; //SPI file
25   char filename[30]; //SPI file name space
26   int loopcount = 0; //for data export
27   int dout; //for data export
28   float current; //current position
29   float max; //max position for finger
30
31   void PISinC1()
32   {
33       desired = -.5*max*cos(.314159265*t)+.5*max; //sin input
34       er0 = desired - pos1; //error
35       eri = eri + ((er0+er)*period)/2.0; //integral
36       er = er0; //stores value
37       PWM = (eri * ki) + (er0 * kp); //control law
38       if(PWM>0) { //assigns direction
39           dr = 1;
40       } else {
41           dr = 0;
42       }
43       st = abs(PWM)+.53; //assigns speed
44       t = t + period; //time
45       loopcount = loopcount + 1; //for data export
46       if( loopcount == 10) {
47           if(PWM>0) {
48               signal = (PWM + .53)*1000;
49           } else {
50               signal = (PWM - .53)*1000;
51           }
52           e = pos1*1000.0;
53           dout = desired*1000.0;
54           fprintf(fp, "%d,%d,%d\n\r",e,signal,dout);
55           loopcount = 0;
56       }
57   }
58
59
60   int main()
61   {
62       getchar(); //get character to start
63       NVIC_SetPriority(TIMER3_IRQn, 1); //assigns ticker priority
64       st.period(.00005); //PWM period
65       for(int i = 1; i < 13; i++) { //do PI control 13 times
66           wait(.1);
67           en = 1;
68           st = 0;
```

```
69              dr = 0;
70              while(touch < .22) { //takes pressure off
71                  wait(.01);
72                  st = .75;
73              }
74              dr = 1;
75              wait(.01);
76              st = 0;
77              wait(.3);
78              printf("Ready");
79              en = 1;
80              max = .59; // max of sin
81              sprintf(filename, "/sd/Fig%d.txt", i); //open file
82              fp = fopen(filename, "w");  // open for writing
83              eri = 0; //reset values
84              er = 0;
85              t = 0;
86              loopcount = 0;
87              c.attach(&PISinC1,period); //do control
88              wait(40); //for 40 s
89              c.detach(); //stop
90              fclose(fp); //close file
91              st = 0; //stop motor
92              en = 0;
93          }
94  }
95
```
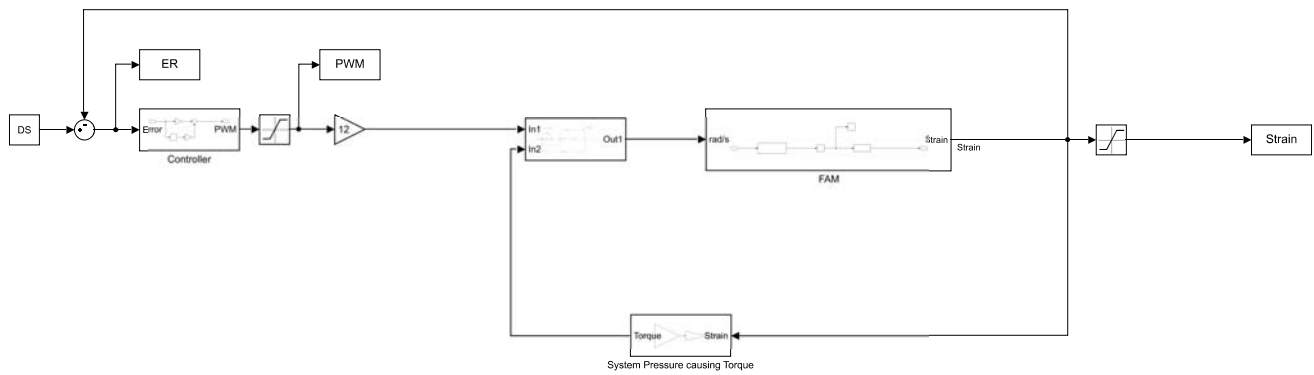
A.3   PI simulation script
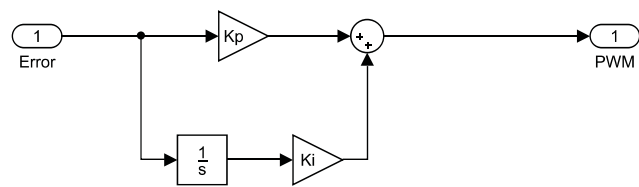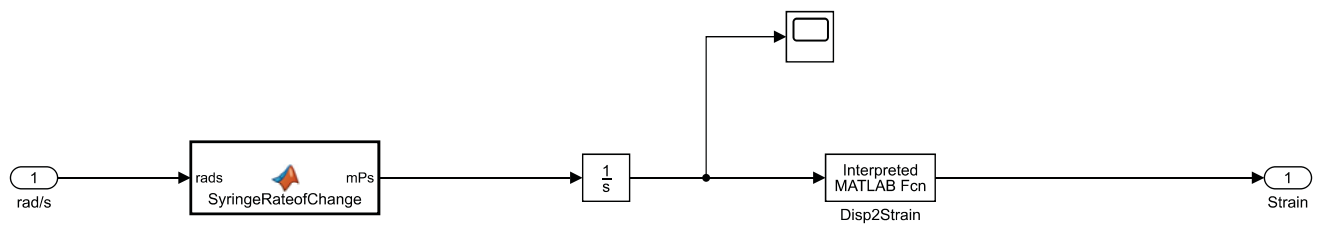
```
1   clear
2   Ra = 4.5;      %Measured
3   La = 0.2835; %Inductance measured
4   kt = .24;    %motor torque constant
5   kb = kt;      %motor back emf constant
6   B = .0001;    %crital damping
7   J = 1.96e-6; %Cylinder on axis 1.96e-6
8   TorqueApprox = 2300;     %conversion of strain to pressure tuned experimentally
9   SyringeArea = (.013^2)*pi;  %Area of the syringe plunger
10  Lt = .254;    %pitch of screw
11  e = .25;      %Efficency based on EXP tuning.
12  LeadScrewFactor = Lt/(2*pi*e); %approximate equation relating force on a lead screw to
    torque on that lead screw
13
14  DS = .2;
15  % Kp = 2.35;
16  % Ki = .28;
17  Kp = 2.35;
18  Ki = .28;
19  sim('VolumeBasedControl'); %run simulation
20  save('PISin_Sim','PWM','Strain','tout');
21  figure(1) %below is plotting
22  subplot(2,1,1)
23  plot(tout,Strain,'k')
24  hold on
25  for i = 1:length(tout)
26      Dsarray(i) = DS;
27  end
28  plot(tout,Dsarray,'r--')
29  h=fill([0,20,20,0],[DS*.98,DS*.98,DS*1.02,DS*1.02],'red','LineStyle','none');
30  h.FaceAlpha=0.3;
31  axis([0 40 0 .25])
32  title('Model Response to PI Control')
33  xlabel('Time (s)')
34  set(findall(gcf, '-property', 'FontSize'),'FontSize',14);
35  ylabel('Strain (cm/cm)')
36  set(findall(gcf, '-property', 'FontSize'),'FontSize',30);
37  set(findall(gca, '-property', 'linewidth'),'linewidth',3);
38  legend({'Model Response','Desired Output'},'Location','SouthEast')
39  grid on
40  subplot(2,1,2)
41  plot(tout,PWM+.53);
42  axis([0 40 -1 1])
43  grid on
44  title('PI Control Output')
45  xlabel('Time (s)')
46  set(findall(gcf, '-property', 'FontSize'),'FontSize',14);
47  ylabel('PWM')
48  set(findall(gcf, '-property', 'FontSize'),'FontSize',30);
49  set(findall(gca, '-property', 'linewidth'),'linewidth',3);
50  %legend({'Model Response','Desired Output'},'Location','SouthEast')
51  % subplot(3,1,3)
52  % plot(tout,ER);
53  % axis([0 10 -.05 .2])
54  % grid on
55  % title('PI Control Error')
56  % xlabel('Time (s)')
57  % set(findall(gcf, '-property', 'FontSize'),'FontSize',14);
58  % ylabel('Error (cm/cm)')
59  % set(findall(gcf, '-property', 'FontSize'),'FontSize',30);
60  % set(findall(gca, '-property', 'linewidth'),'linewidth',3);
61  % %legend({'Model Response','Desired Output'},'Location','SouthEast')
```
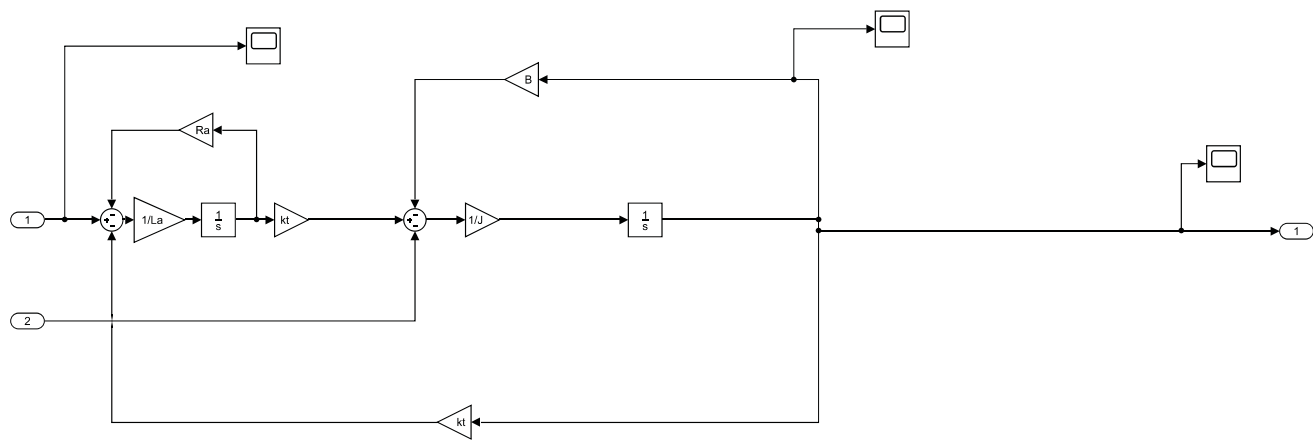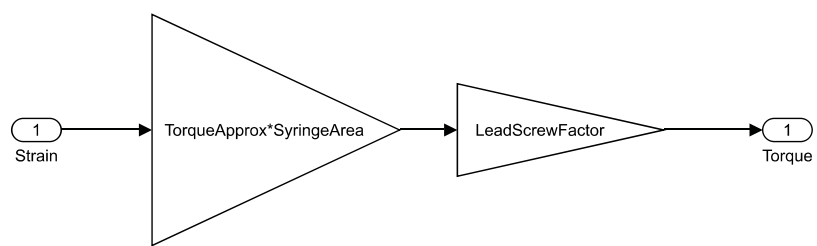
A.4   PI Simulink

1

rad/s

rads mPs

SyringeRateofChange

$\frac{1}{s}$

Interpreted
MATLAB Fcn

Disp2Strain

1

Strain

```
function mPs = SyringeRateofChange(rads)
mPs = rads*.00254/(2*pi);
```

1

1/La

1/s

kt

Ra

2

1/J

1/s

B

kt

1

```
                                    TorqueApprox*SyringeArea
  ( 1 ) ──────────▶                                          ──▶        LeadScrewFactor        ──▶  ( 1 )
  Strain                                                                                            Torque
```
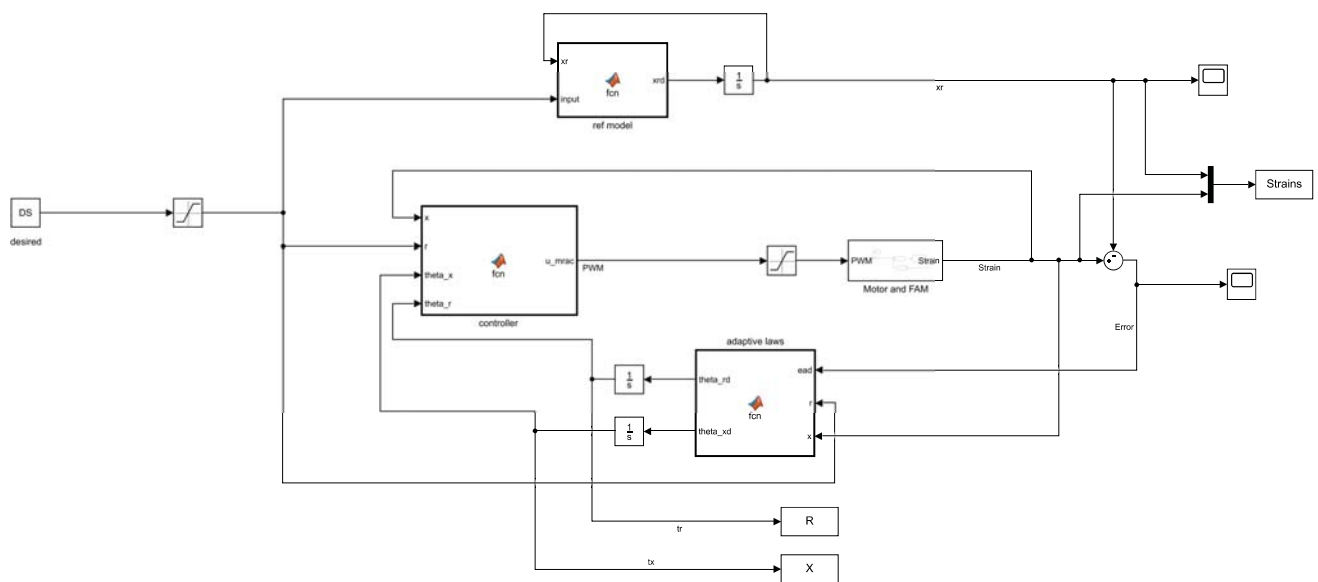
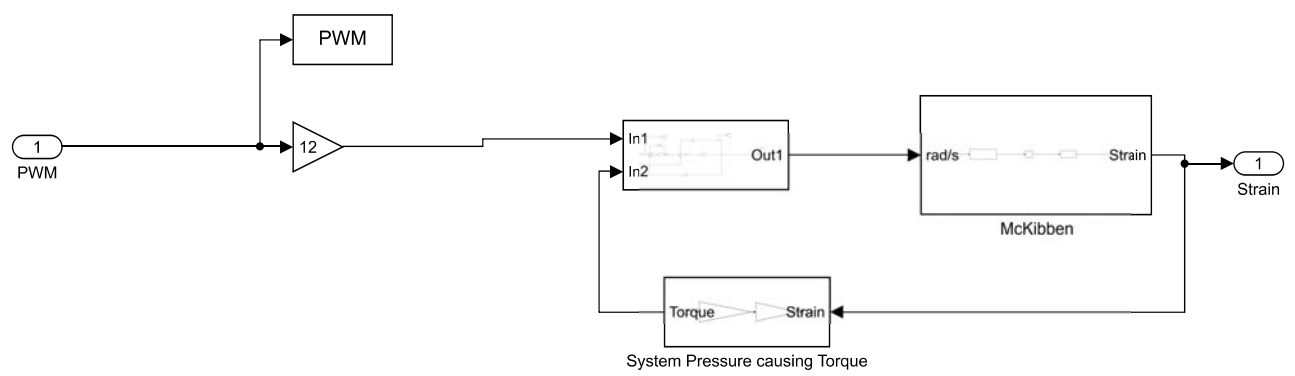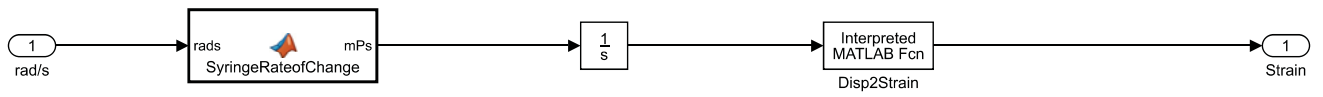## A.5   MRAC simulation script

```
1    clear
2    br = .5;    %for reference system
3    kr0 = 2;    %inital gain conditions
4    kx0 = -2;
5    gx = 900;  %gain rate of change
6    gr = 1000;
7    Ra = 4.5;     %Measured
8    La = 0.2835; %Inductance measured
9    kt = .24;    %motor torque constant
10   kb = kt;     %motor back emf constant
11   B = .0001;
12   J = 1.96e-6; %Cylinder on axis
13   TorqueApprox = 2300;     %conversion of strain to pressure tuned experimentally
14   SyringeArea = (.013^2)*pi;  %Area of the syringe plunger
15   Lt = .254;   %pitch of screw
16   e = .25;     %Efficency based on EXP tuning.
17   LeadScrewFactor = Lt/(2*pi*e); %approximate equation relating force on a lead screw to
     torque on that lead screw
18   Fs = 0;
19
20   DS = .2;     %Desired strain
21   sim('VolumeMRAC')%run simulation
22   figure(1) %Below is plotting
23   clf
24   subplot(2,1,1)
25   plot(tout,Strains(:,2),'k')
26
27   hold on
28   plot(tout,Strains(:,1),'r--')
29   title('Model Response to MRAC')
30   xlabel('Time (s)')
31   set(findall(gcf, '-property', 'FontSize'),'FontSize',14);
32   ylabel('Strain (cm/cm)')
33   set(findall(gcf, '-property', 'FontSize'),'FontSize',30);
34   set(findall(gca, '-property', 'linewidth'),'linewidth',3);
35   legend({'Model Response','Desired Output'})
36   grid on
37   subplot(2,1,2)
38   plot(tout,PWM);
39   axis([0 120 -1 1])
40   grid on
41   title('PI Control Output')
42   xlabel('Time (s)')
43   set(findall(gcf, '-property', 'FontSize'),'FontSize',14);
44   ylabel('PWM')
45   set(findall(gcf, '-property', 'FontSize'),'FontSize',30);
46   set(findall(gca, '-property', 'linewidth'),'linewidth',3);
47   figure(2)
48   clf
49   plot(tout,R)
50   hold on
51   plot(tout,X)
52   title('Model Response to MRAC: Gains')
53   xlabel('Time (s)')
54   set(findall(gcf, '-property', 'FontSize'),'FontSize',14);
55   ylabel('Magintude')
56   set(findall(gcf, '-property', 'FontSize'),'FontSize',30);
57   set(findall(gca, '-property', 'linewidth'),'linewidth',3);
58   legend({'{\theta_r}','{\theta_x}'})
59   grid on
60   save('MRACRamp_Sim','PWM','Strains','tout','R','X');
```
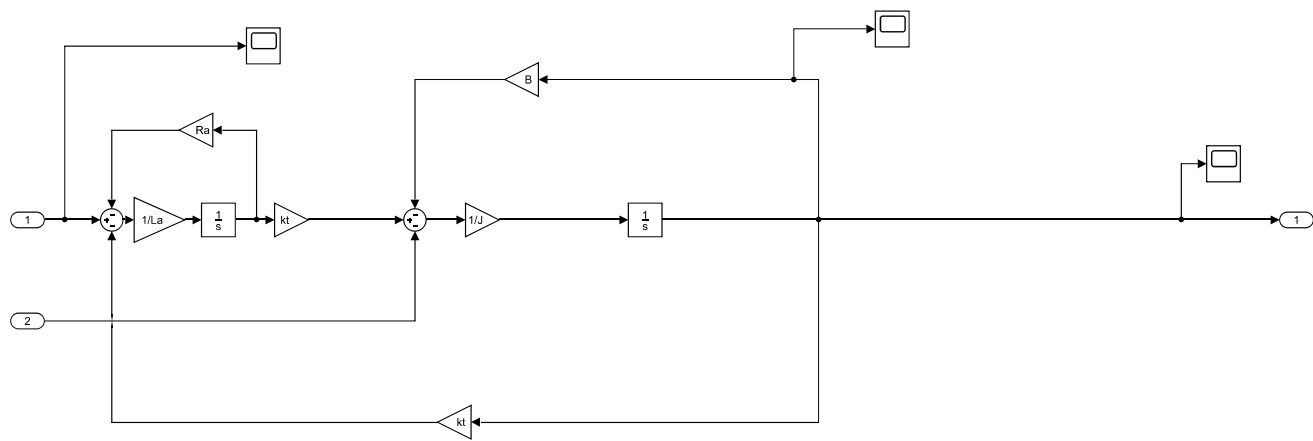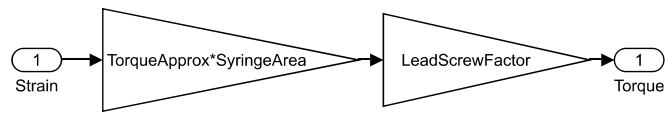
A.6 MRAC Simulink

PWM

PWM

12

In1
In2
Out1

rad/s   Strain

McKibben

Torque   Strain

System Pressure causing Torque

1

Strain

```
function mPs = SyringeRateofChange(rads)
mPs = rads*.00254/(2*pi);
```

```
        1  ──▶  ⟨ TorqueApprox*SyringeArea ⟩  ──▶  ⟨ LeadScrewFactor ⟩  ──▶  1
      Strain                                                                Torque
```

```
function [theta_rd, theta_xd] = fcn(ead,r,x, br,gx,gr)
%#codegen
%deleted b


theta_xd = -gx*ead*x*sign(br);

theta_rd = -gr*ead*r*sign(br);
```

```
function u_mrac = fcn(x, r, theta_x, theta_r)
%#codegen

u_mrac = theta_x*x+theta_r*r;
```

```
function xrd = fcn(xr,input,br)
%#codegen

ar = -br;
xrd = ar*xr + br*input;
```

A.7 Mathematical implementation of fixed-end model

```
1   function [S] = Disp2Strain(d)
2    S = real ((- 0.090075 - 0.15602i)/(5.6883*d + ((5.6883*d - 0.010049)^2 -
     0.0058467)^(1/2) - 0.010049)^(1/3)...
3    - (5.6883*d + ((5.6883*d - 0.010049)^2 - 0.0058467)^(1/2) - 0.010049)^(1/3)*(0.5 -
     0.86603i) + 0.75309);
4   end
```